



Aerosols heat up the Himalayan climate

S. Ramachandran^{a,b,*}, Maheswar Rupakheti^b, Ribu Cherian^c, Mark G. Lawrence^{b,d}

^a Physical Research Laboratory, Ahmedabad, India

^b Research Institute for Sustainability – Helmholtz Centre Potsdam, Potsdam, Germany

^c Leipzig Institute for Meteorology, University of Leipzig, Leipzig, Germany

^d Institute for Environmental Sciences and Geography, University of Potsdam, Potsdam, Germany

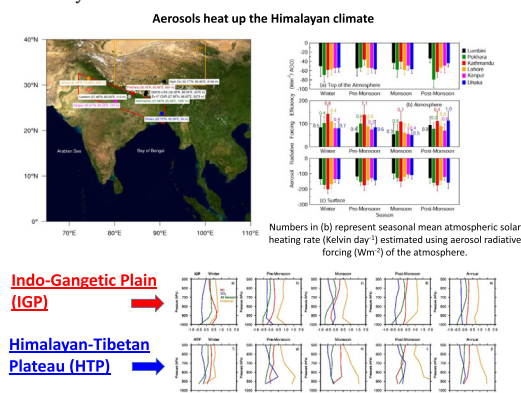


HIGHLIGHTS

- First time, aerosol radiative forcing and efficiency (ARFE) over Himalayas quantified
- ARFE is high (80–135 Wm⁻² per unit aerosol optical depth) over Himalayas.
- Enhanced warming is likely contributing to elevated trend in temperature in Himalayas.
- Aerosols alone account for >50 % of the total warming of lower atmosphere.
- Aerosols are, and will remain a key factor driving climate change over the Himalayas.

GRAPHICAL ABSTRACT

Temperature change (K) due to aerosols and greenhouse gases in the lower atmosphere over the IGP and the HTP simulated by UKESM1.



ARTICLE INFO

Editor: Pavlos Kassomenos

Keywords:

Atmospheric aerosols
Radiative effects
Observations
Model simulations
Himalayas
South Asia

ABSTRACT

The impact of aerosols, especially the absorbing aerosols, in the Himalayan region is important for climate. We closely examine ground-based high-quality observations of aerosol characteristics including radiative forcing from several locations in the Indo-Gangetic Plain (IGP), the Himalayan foothills and the Tibetan Plateau, relatively poorly studied regions with several sensitive ecosystems of global importance, as well as highly vulnerable large populations. This paper presents a state-of-the-art treatment of the warming that arises from these particles, using a combination of new measurements and modeling techniques. This is a first-time analysis of its kind, including ground-based observations, satellite data, and model simulations, which reveals that the aerosol radiative forcing efficiency (ARFE) in the atmosphere is clearly high over the IGP and the Himalayan foothills (80–135 Wm⁻² per unit aerosol optical depth (AOD)), with values being greater at higher elevations. AOD is >0.30 and single scattering albedo (SSA) is ~0.90 throughout the year over this region. The mean ARFE is 2–4 times higher here than over other polluted sites in South and East Asia, owing to higher AOD and aerosol absorption (i.e., lower SSA). Further, the observed annual mean aerosol-induced atmospheric heating rates (0.5–0.8 Kelvin/day), which are significantly higher than previously reported values for the region, imply that the aerosols alone could account for >50 % of the total warming (aerosols + greenhouse gases) of the lower atmosphere and surface over this region. We demonstrate that the current state-of-the-art models used in climate assessments significantly underestimate aerosol-induced heating, efficiency and warming over the Hindu Kush – Himalaya – Tibetan Plateau (HKHTP) region, indicating a need for a more realistic representation of aerosol properties, especially of black carbon and other aerosols. The significant, regionally coherent aerosol-induced warming that we observe in the high altitudes of the region, is a significant factor contributing to increasing

* Corresponding author at: Physical Research Laboratory, Ahmedabad, India.
E-mail addresses: ram@prl.res.in, srikanthan.ramachandran@rifs-potsdam.de (S. Ramachandran).

<http://dx.doi.org/10.1016/j.scitotenv.2023.164733>

Received 17 March 2023; Received in revised form 4 June 2023; Accepted 6 June 2023

Available online 14 June 2023

0048-9697/© 2023 The Authors. Published by Elsevier B.V. This is an open access article under the CC BY-NC-ND license (<http://creativecommons.org/licenses/by-nc-nd/4.0/>).

air temperature, observed accelerated retreat of the glaciers, and changes in the hydrological cycle and precipitation patterns over this region. Thus, aerosols are heating up the Himalayan climate, and will remain a key factor driving climate change over the region.

1. Introduction

The main observable aerosol characteristics - mass concentration, chemical composition and optical properties - exhibit a wide variability across locations and seasons. This is especially the case in southern Asia, due to the large and regionally-varying sources, complex geophysical setting and the monsoon seasonal dynamics (IPCC, 2021). The Hindu Kush – Himalayan – Tibetan Plateau (HKHTP) mountain region stretches across eight countries in South Asia from Afghanistan to Myanmar including Pakistan, India, China, Bangladesh, Bhutan and Nepal, and exhibits significant heterogeneity in terms of landscape, precipitation, vegetation, development, and livelihoods (Sharma et al., 2019). Aerosol emissions, especially the anthropogenic emissions, are changing rapidly over Asia (Samset et al., 2019). The recent changes in aerosol emissions over Asia, with the emissions increasing over South Asia and decreasing over East Asia, have resulted in a dipole in aerosol pollution and its radiative effects between South Asia and East Asia (Samset et al., 2019; Ramachandran et al., 2020a). Current climate models with state-of-the-art representation of physical and chemical processes grossly underestimate aerosol absorption in many regions, especially over Asia (Shindell et al., 2013; Myhre et al., 2017; Ramachandran et al., 2022; IPCC, 2021). Black carbon (BC), brown carbon (BrC), and dust are the three absorbing aerosol types. BC and BrC are co-emitted during open biomass burning, open garbage burning, domestic biomass combustion (cooking and heating), and fossil fuel combustion. Mineral dust from deserts and arid regions is transported to the Himalayan region from different origins upwind by the summer and winter monsoon winds. Among these three, it has been shown that the BC aerosol dominates ($\geq 75\%$) the aerosol absorption over the Indo-Gangetic Plain (IGP) and the Himalayas throughout the year (Ramachandran et al., 2020b). The aerosol absorption over South Asia was also found to be very high, exceeding the available observations over East Asia (Ramachandran et al., 2020b; Ramachandran and Rupakheti, 2022).

An analysis of a two-decade-long time series of observations of aerosol properties from the ground-based Aerosol Robotic Network (AERONET), satellites (Moderate Resolution Imaging Spectroradiometer (MODIS) and Ozone Monitoring Instrument (OMI)), and model simulations (Modern-Era Retrospective Analysis for Research and Applications, version 2 (MERRA-2), over Kanpur in the IGP (South Asia) and Beijing in the North China Plain (NCP) (East Asia), two locations taken as being broadly representative of the South and East Asia, respectively, revealed a dipole in aerosol optical depth (AOD) - an increase in AOD over South Asia and a decrease over East Asia, with a rapid decrease over East Asia since 2010 (Ramachandran et al., 2020a). The single scattering albedo (SSA), a measure of aerosol's absorption capacity and related to aerosol composition, had increased over both regions, confirming that aerosols in this region have become more scattering and less absorbing in nature. The IGP in South Asia and the NCP in East Asia are characterized mainly by emissions from fossil fuel combustion and biomass burning during all seasons, along with desert dust events that occur primarily in the spring season (March–May) and contribute to the heavy aerosol pollution. The IGP and the NCP are influenced by the Asian summer monsoonal dynamics, with northeasterly and southwesterly winds during the winter and summer monsoon, respectively. It was found that the seasonal trends in aerosol characteristics were caused mainly by the changes in anthropogenic aerosol emissions (sulfate, black carbon and organic carbon) while the natural aerosols (dust and sea salt) did not vary significantly over South and East Asia during the last two decades (Ramachandran et al., 2020a). The annual-mean aerosol-induced atmospheric heating (due to light-absorbing aerosols)

was found to be quite large (>0.5 K) over Asia, which has significant implications for the climate and hydrological cycle (Ramachandran et al., 2020a).

The HKHTP region is observed to have warmed significantly in the past decades, with the magnitude of warming being higher than the global-mean value (Krishnan et al., 2019). The observed warming here is higher in magnitude than the averages for the Northern Hemisphere and the same latitudinal zone. The warming over this region continued even during the global warming hiatus, and increased with elevation in this region (Krishnan et al., 2019). The light-absorption by BC aerosols, which are dominant over this region, can further enhance the regional warming and accelerate snowmelt (Ramachandran et al., 2020b). Consequently, the glaciers in the HKHTP region, known as the third pole, may lose as much as two-thirds of ice by the end of the century due to climate change (Sharma et al., 2019; Kang et al., 2020). This is a serious issue as water that flows downstream from its ten rivers is the lifeline for about 250 million inhabitants directly in the HKHTP region and >1.5 billion people benefit further downstream (Sharma et al., 2019). In addition, absorbing aerosols can enhance the snow-albedo feedback and the Indian summer monsoon, result in extreme precipitation, and pose a threat to human lives (Yuan et al., 2021). A related issue is the air pollution over the HKHTP that arises within the region and in upwind regions, from diverse sources such as cooking stoves, brick kilns, other industries, power plants and transport. The air pollution levels here are on the rise and exhibit significant seasonal and regional variation (Saikawa et al., 2019). During winter the haze and fog occurrences have increased across the adjacent IGP, resulting in reduced visibility and affecting air quality in the IGP as well as the HTP mountain regions (Saikawa et al., 2019). The magnitudes and sign of regional aerosol radiative forcing (ARF) of the climate, especially from anthropogenic aerosols, are still highly uncertain, especially because the IGP and the downwind regions that receive the pollution outflow, such as the HTP mountain regions, remain poorly sampled (Lawrence and Lelieveld, 2010; Ramachandran et al., 2020a, 2020b). Models tend to underestimate observed BC mass concentrations in the southern Asian pollution outflow region (Lawrence and Lelieveld, 2010). As a result, models significantly underestimate aerosol absorption in this region (Koch et al., 2009; Ramachandran et al., 2022) as well. BC mass concentrations over south Asia simulated by two models – MERRA-2 (at a finer latitude-longitude resolution of $0.5^\circ \times 0.625^\circ$) and the European Centre for Medium-Range Weather Forecasts-Hamburg (ECHAM6) extended by Hamburg Aerosol Module-2 (HAM2) (at a coarser latitude-longitude resolution of $1.8^\circ \times 1.8^\circ$) – were significantly lower than the observations. This indicates that BC and its long range transport were inadequately represented in the models, in particular over the source regions, strongly suggesting that improvements in emission inventories of aerosol sources as well as inclusion of missing aerosol source categories are needed (Ramachandran et al., 2021). More recently, analysis of comparison between collocated AERONET observations and MERRA-2 simulations showed that the total aerosol loading and aerosol composition simulated by MERRA-2 were less accurate than ground-based AERONET observations during winter season when BC aerosols dominate the IGP (Ansari and Ramachandran, 2023). Further, it was observed that the correlation between collocated AERONET and Copernicus Atmosphere Monitoring Service (CAMS) model simulated AODs (at a latitude-longitude resolution of $0.75^\circ \times 0.75^\circ$) over the IGP was better, and a major reason for the better performance of the CAMS model is because it utilizes the recent and updated emission inventories related to anthropogenic aerosols (Ansari and Ramachandran, 2023). Unlike the other mountain regions, accurately simulating the present climate and radiative effects over the HKHTP region is

of great significance owing to its crucial importance in terms of the regional and global climate, environment, agriculture, health and livelihood. This becomes highly critical for predicting the future climate and impacts, developing plans to mitigate climate change and air pollution (especially aerosols), and supporting efforts to meet the sustainable development goals (SDGs).

Studies during the last decade have documented the variations in aerosol characteristics and ARF over this region (Ramanathan et al., 2007a; Lawrence and Lelieveld, 2010; Kedia et al., 2014; Cho et al., 2017). Most studies (except the few reviews) have focused on observations from a particular season and/or a particular location. In this context, the primary motivations of the study were to analyze the South Asian aerosol characteristics including the absorbing aerosols, to determine aerosol radiative effects and how they vary temporally and regionally, and to provide observational constraints for the aerosol-induced atmospheric warming and consequent climate impact across the IGP and the HTP region, a global aerosol hotspot region. The ground-based observed ARF is compared with values derived from satellite data and with the state-of-the-art climate model used in the recent IPCC AR6 (IPCC, 2021). The vertical profile of atmospheric warming due to aerosols in the lower troposphere is assessed for each season. This paper presents a first-of-its-kind state-of-the-art treatment of the warming that arises from these particles, using a combination of new

high-quality measurements, and modeling techniques. This rigorous analysis enabled us to apportion the warming effects due to aerosols and other greenhouse gases over the large regional domain on spatial and temporal scales. This study based on the analysis of observations and model simulations documents the altitude-dependent influence of aerosol radiative effects over the Himalayas, which is very likely contributing to the elevated trends in air temperature, elevation-dependent warming (EDW) and the observed accelerated retreat of the glaciers over the climate-sensitive HKHTP region, and also discusses the climate implications. The study is novel as it combines data from multiple sources – high-quality ground-based observations along with satellite data in combination with global climate simulations – to document the aerosol radiative effects as a function of space, time and altitude over this region.

2. Study region

The IGP (Fig. 1), that covers parts of Pakistan, India, Bangladesh and Nepal, is a densely populated, industrialized and a heavily polluted region in South Asia (Ramanathan et al., 2007b). Diverse aerosol emissions from natural and anthropogenic sources (dust, BC, nitrate, sulfate and organics) give rise to a persistent blanket of haze characterized by heavy aerosol loading over the IGP and downwind regions throughout nearly the whole year

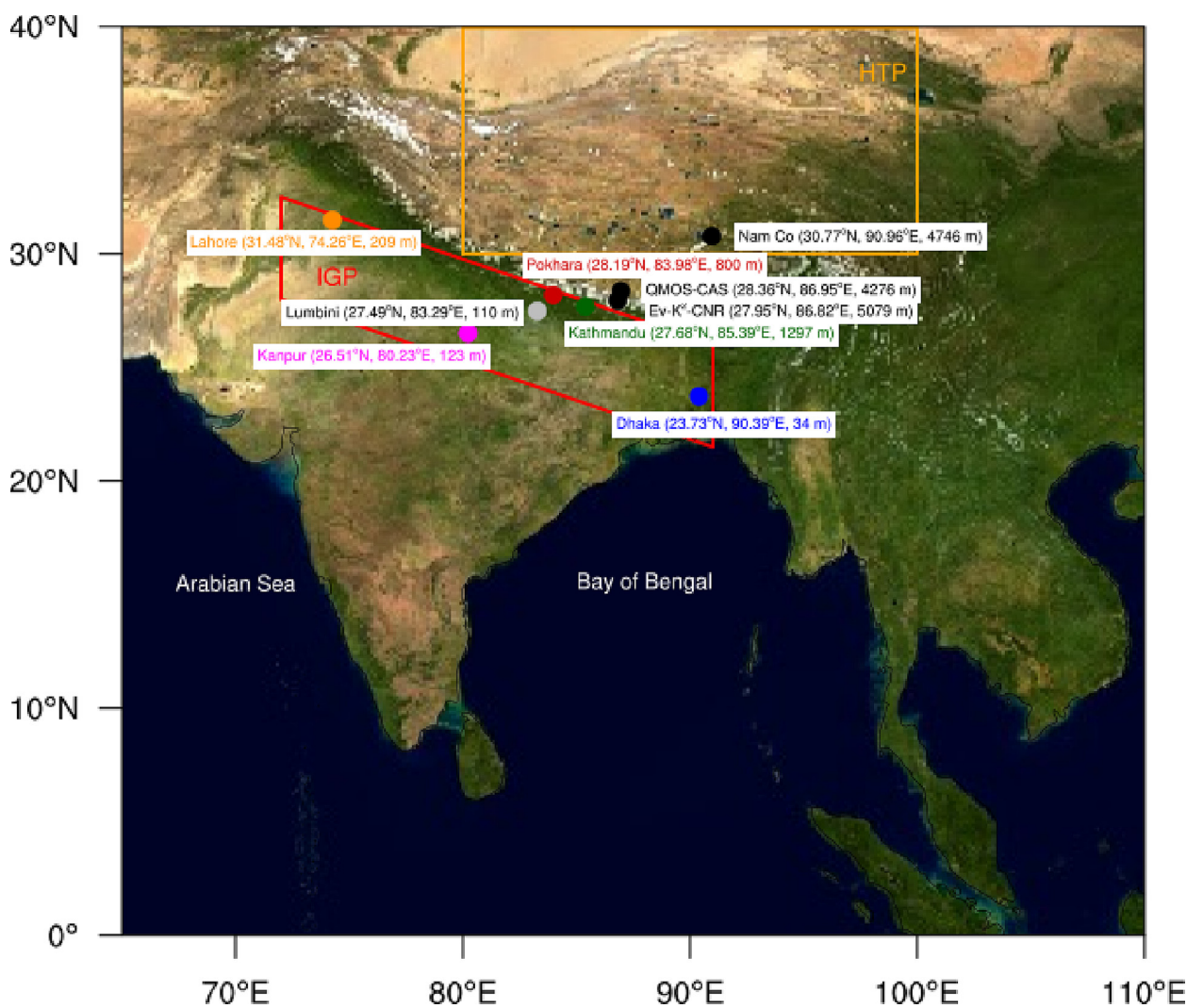


Fig. 1. Details of the locations of observation sites in the Indo-Gangetic Plain (IGP) and the Himalayan foothills in South Asia: The latitude, longitude, and elevation (in meters above sea level, m asl) of each location are given. Four observation sites - Lahore (Pakistan), Kanpur (India), Lumbini (Nepal) and Dhaka (Bangladesh) - are located along a northwest-southeast transect of the IGP, while three sites (Lumbini, Pokhara and Kathmandu in Nepal) are located at increasing altitudes from the northern edge of the IGP to the Himalayan foothills. The domains of the IGP and HTP are drawn in the map.

(Ramanathan et al., 2007b; Xu et al., 2016; Maurer et al., 2019; Sharma et al., 2019; Kedia et al., 2014) (Fig. 2). The observation sites are located in the IGP and the central Himalayan foothills (Figs. 1, 2, Table 1). Lahore, Kanpur and Dhaka are urban, industrial and densely populated cities with heavy air pollution. Kanpur is located ~500 km east of the megacity New Delhi. Lumbini is a rural area at the northern edge of the IGP. The Kathmandu Valley and Pokhara Valley in the central Himalayas, are two major metropolitan regions in the foothills of the Hindu Kush Himalaya mountains (the largest and second largest metropolitan regions, respectively, in Nepal). The three sites in Nepal are distinct in terms of their elevation and environment, and in terms of the downwind influence of the IGP (Fig. 1, Table 1). On a regional scale, all six locations are influenced by the southern Asian monsoon system, with northeasterly winds during winter and southwesterly during the summer monsoon (Fig. 3) (Ramanathan et al., 2007a; Kedia et al., 2014).

3. Materials and methods

3.1. Ground-based aerosol data

The level 2, version 3 cloud screened and quality assured daily data of aerosol optical depth (AOD), single scattering albedo (SSA), fine mode fraction (FMF), aerosol radiative forcing (ARF) and aerosol radiative forcing efficiency (ARFE) from the NASA Aerosol Robotic Network (AERONET) using ground-based CIMEL Sun/sky radiometers (Holben et al., 2001) which measure direct solar and diffuse sky radiances in the spectral range of 0.34–1.02 μm , for a period of a year over Lumbini (Jan–Aug 2013 and Sep–Dec 2017), Pokhara (Jan–Dec 2012) and Bode, Kathmandu (Jan–Mar, Jul–Dec 2013 and Apr–Jun 2014) (all in Nepal), and Lahore (Pakistan) (Jan–Dec 2012), Kanpur (India) (Jan–Dec 2012), and Dhaka (Jan–Dec 2014) are utilized. As the objective is to cover one annual cycle over all the study locations, data sets corresponding to years 2013–14, and 2012 (when data were not available) were utilized. The years 2012–14 were chosen as the coincident data was available for almost all the months at most

locations in this timeframe. This approach of usage and analysis of the data available either in the preceding year(s), and/or the subsequent year (s) with respect to the preferred chosen year(s) is quite appropriate in this case, and is not expected to influence the resultant scientific outcomes significantly because (a) all the data are from the same instrument which have undergone the same level of quality-control and cloud-screening, (b) aerosol characteristics exhibit more prominent seasonal variations than inter-annual variations (Lawrence and Lelieveld, 2010; Kedia et al., 2014; Ramachandran et al., 2015), (c) any effect of continued increase/decrease in natural and/or anthropogenic activity is expected to be minimal as the AODs did not show any noticeable increase or decrease over a 5-year period (e.g., Ramachandran et al., 2015 and references therein), and (d) finally, the changes in aerosol concentrations due to changes/variations in meteorology over a 5-year period were relatively small (Zhang et al., 2019). Depending on the prevailing meteorological conditions over the IGP, analyzed data are classified into four seasons as winter (December–February), pre-monsoon (March–May), monsoon (June–September) and post-monsoon (October–November) (Fig. 3).

The level 2, version 3 algorithm of AERONET has been updated relative to the previous version to include improved cloud screening and quality control methods, cirrus cloud detection and removal (Giles et al., 2019). The newly added cirrus cloud-screening quality control check in this version was found to decrease the probability of a cirrus bias globally (Giles et al., 2019). Aerosol properties corresponding to individual observations (made at 15–20 min time intervals), and typically about 20 daily measurements during the chosen year(s) are used to calculate the monthly, seasonal and annual averages, and are utilized in the present work. The AERONET retrieved aerosol properties have the highest accuracy for observations when solar zenith angle is between 50° and 80° (Dubovik et al., 2000), and only those data points in a day that are within this solar zenith angle range are utilized in the study. The uncertainty in AODs calculated using the direct solar radiation measurements is less than ± 0.01 for wavelengths $>0.44 \mu\text{m}$ and is less than ± 0.02 for shorter wavelengths (Holben et al., 2001). The error in SSA is ± 0.03 when the AOD at $0.44 \mu\text{m}$ is >0.2

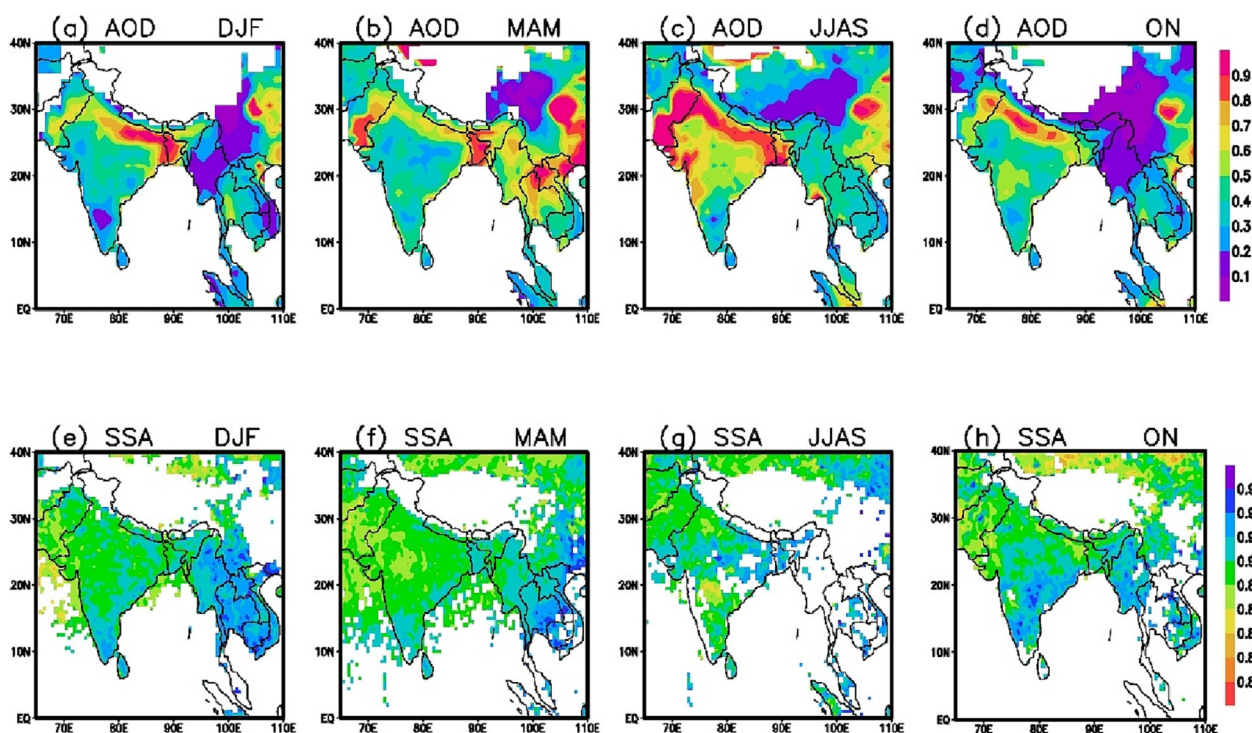


Fig. 2. Spatial and seasonal variations in satellite retrieved aerosol optical depth and single scattering albedo. Seasonal mean MODIS aerosol optical depth (AOD) at a wavelength of $0.55 \mu\text{m}$ for (a) winter, (b) pre-monsoon, (c) monsoon and (d) post-monsoon 2012, and OMI OMAERO v003 single scattering albedo (SSA) at a wavelength of $0.388 \mu\text{m}$ for (e) winter, (f) pre-monsoon, (g) monsoon and (h) post-monsoon 2012. Data downloaded from <https://giovanni.gsfc.nasa.gov/giovanni/>.

Table 1

Details of the study locations (latitude, longitude and elevation in meters (m) above mean sea level (asl)), and surface albedo at each location. The spectral average of surface albedo is given (along with $\pm 1\sigma$ standard deviation) at each location in the Himalayan foothills and the Indo-Gangetic Plain during each season (DJF (winter), MAM (pre-monsoon), JJAS (monsoon) and ON (post-monsoon)), as utilized in the present study.

Location	DJF	MAM	JJAS	ON
Himalayan foothills:				
1. Lumbini, Nepal (27.5°N, 83.3°E, 110 m)	0.21 \pm 0.02	0.22 \pm 0.02	0.25 \pm 0.02	0.22 \pm 0.02
2. Pokhara, Nepal (28.2°N, 83.9°E, 800 m)	0.14 \pm 0.01	0.16 \pm 0.01	0.18 \pm 0.01	0.16 \pm 0.01
3. Kathmandu, Nepal (27.7°N, 85.4°E, 1297 m)	0.15 \pm 0.01	0.18 \pm 0.01	0.20 \pm 0.01	0.18 \pm 0.01
Indo-Gangetic Plain:				
4. Lahore, Pakistan (31.4°N, 74.3°E, 209 m)	0.19 \pm 0.02	0.20 \pm 0.01	0.21 \pm 0.02	0.19 \pm 0.02
5. Kanpur, India (26.5°N, 80.2°E, 123 m)	0.22 \pm 0.02	0.23 \pm 0.02	0.24 \pm 0.02	0.22 \pm 0.02
6. Dhaka, Bangladesh (23.7°N, 90.4°E, 34 m)	0.13 \pm 0.01	0.15 \pm 0.01	0.14 \pm 0.01	0.13 \pm 0.01

(Dubovik et al., 2000). The FMF is calculated as the ratio of fine mode AOD (due to particles in 0.01–1.0 μm radius range) to total AOD (due to all particles in 0.01–10.0 μm radius range) at 0.50 μm from sky radiance

measurements. The error in AERONET derived FMF is $\sim 10\%$ (O'Neill et al., 2003). The number of days (daily-average) data sets used in the present study from each location as function of the season (winter (DJF), pre-

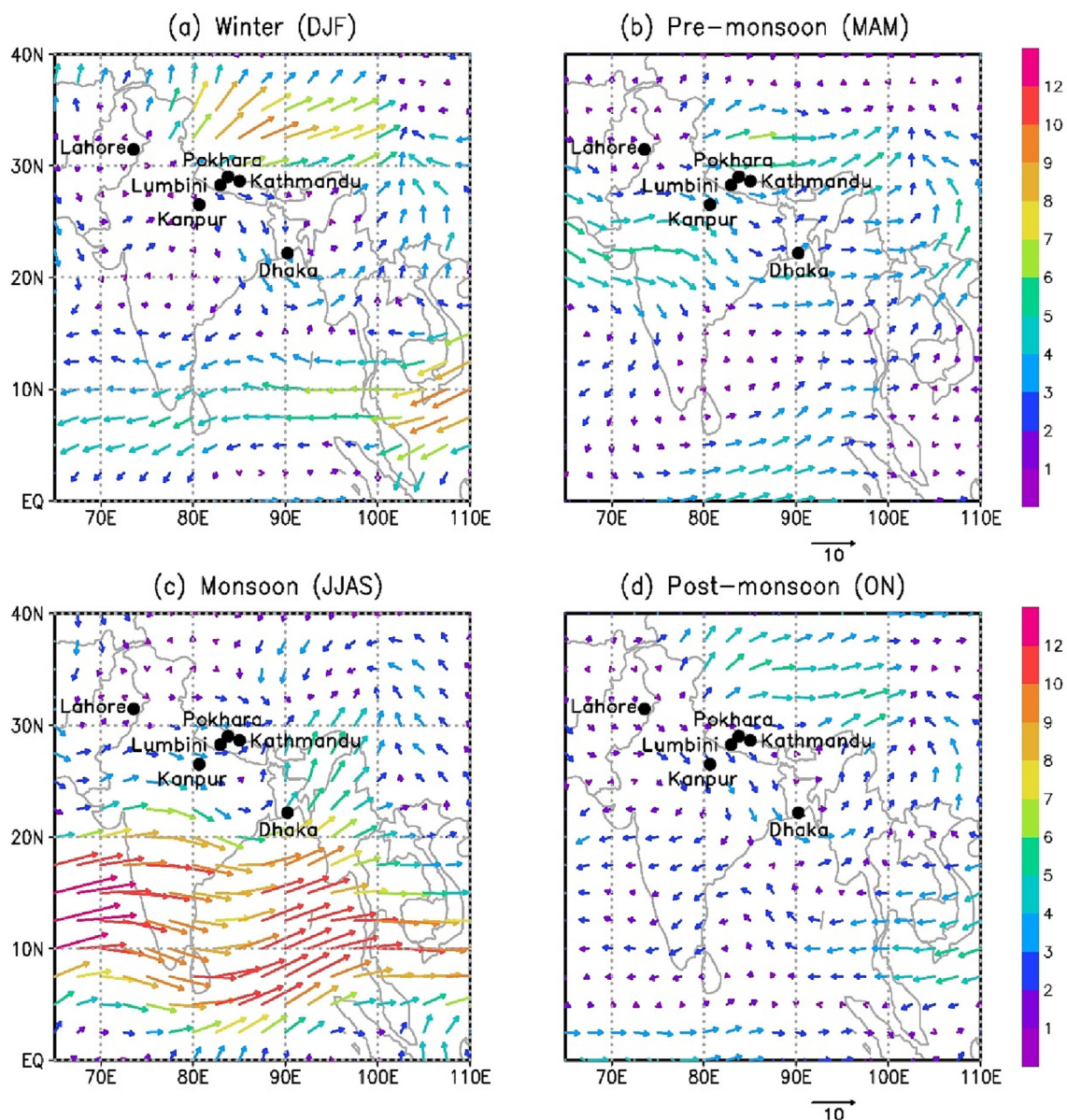


Fig. 3. Seasonal average synoptic winds (in ms^{-1}) at 850 hPa over the Indo-Gangetic Plain and the Himalayan-Tibetan Plateau region during (a) winter (DJF), (b) pre-monsoon (MAM), (c) monsoon (JJAS) and (d) post-monsoon (ON) for 2011–12. Wind data are downloaded from <http://www.esrl.noaa.gov/psd/>. The color scale represents the wind speed, and the length of the arrow given in (b) and (d) correspond to 10 ms^{-1} . Study locations in the Indo-Gangetic Plains and the Himalayan foothills are shown in the plots.

monsoon (MAM), monsoon (JJAS) and post-monsoon (ON)) and total are - Lumbini (45, 78, 48, 48, 224), Pokhara (83, 84, 70, 57, 294), Kathmandu (81, 76, 59, 41, 267), Lahore (58, 82, 107, 56, 303), Kanpur (54, 72, 63, 29, 218), and Dhaka (76, 70, 52, 54, 252). The study region is cloudy and overcast during the monsoon season, as a result of which the cloud screening reduces the number of data points used for analysis during this season, however, the changes in aerosol characteristics are reliable, and are included because the observations during the monsoon also undergo the same level of quality control and cloud screening similar to the other seasons.

Aerosol Radiative Forcing (ARF) depends on AOD, SSA, asymmetry parameter, surface albedo, and relative position of aerosols and clouds as a function of altitude (in case of deriving vertical profiles of ARF), and insolation. Surface albedo plays a crucial role in accurately estimating ARF. The effect of surface albedo on ARF was found to be less critical when surface albedo was <0.30 , and was critical for ARF estimates when surface albedo was >0.30 (García et al., 2012). The AERONET operational data is found to overestimate the ARF data at the surface (ARF_{sfc}) as the upward fluxes with and without aerosols are not taken into account (García et al., 2012). To correct the overestimation, the AERONET ARF_{sfc} needs to be multiplied with $(1-SA)$, where SA is the spectral average of surface albedo (García et al., 2012) which is done in the present study. AERONET retrieval provides surface albedo for each almucantar (almucantar refers to a series of measurements taken at the elevation angle of the Sun for specified azimuth angles relative to the position of the Sun) (Dubovik et al., 2000) retrieval (inversion algorithm product) in a day at the wavelengths of 0.44, 0.675, 0.87 and 1.02 μm . The spectral average of the surface albedo in the wavelength range of 0.44–1.02 μm for all the locations in the current study is <0.30 during the year (Table 1). The surface albedo exhibits spatial and temporal variations – it is higher over Lumbini than Pokhara and Kathmandu in the Himalayan foothills, and in the IGP the surface albedo is higher over Lahore and Kanpur as compared to Dhaka, a coastal location. The surface albedo during the pre-monsoon and monsoon, in general, is higher than the post-monsoon and winter.

The AERONET operational ARFs are instantaneous values, and correspond to the time of measurement which are used to calculate seasonal and annual averages and then used in the present study. The minimum (begin) and the maximum (top) altitudes for flux calculations in AERONET are the elevation of each study location in asl (given in Table 1) and 120 km, respectively. AERONET ARF values (derived for the broadband solar spectrum (0.2–4.0 μm)) are quality controlled, cloud screened, calibrated, and are retrieved for clear-sky atmosphere, and for aerosols present in the column. The aerosol radiative forcing efficiency (ARFE) is defined as the ARF normalized to the AOD at 0.55 μm . The AERONET retrieval algorithm uses a spheroid mixture as a generalized aerosol model (representing spherical, non-spherical, and mixed aerosols) (Dubovik et al., 2006), thereby accounting for non-spherical dust particles. Subsequently the radiation fluxes with aerosols are also modeled using a mixture of spheroids and the detailed phase function (García et al., 2008), though the influence of particle shape on ARF is negligibly small (Mishchenko et al., 1997). The AERONET flux simulation relies on the retrieved real and imaginary parts of refractive index. The spectral integration uses real and imaginary parts of the refractive index which are interpolated or extrapolated from the values of refractive index retrieved at AERONET wavelengths. The AERONET retrieval of flux calculations account for absorption and multiple scattering effects (Dubovik et al., 2006; García et al., 2008). The radiative transfer calculations for gaseous absorption is performed using radiative transfer model GAME (Global Atmospheric Model) (Dubuisson et al., 1996) in which spectral integration is performed using correlated-k distribution based on line-by-line simulations. The instantaneous water vapor content retrieved by AERONET is utilized and ozone content is taken from the NASA TOMS ozone climatology (García et al., 2008). The GAME model accounts for spectral gaseous absorption, for example, ozone in the UV–visible wavelength range, and water vapor in the shortwave IR spectrum (García et al., 2008). The atmosphere is assumed to be plane-parallel in AERONET retrievals, and

the vertical distribution of aerosols is assumed to be homogeneous in the almucantar inversion, and bi-layered for the principal plane inversion (Dubovik et al., 2006). The US standard 1976 atm model is scaled to match the atmospheric gaseous concentrations in the column and employed. The uncertainty/error in the AERONET calibrated sky radiance measurements is $\sim 5\%$ (Dubovik and King, 2000).

The AERONET retrievals are found to be adequately sensitive to observe important minor features in spectral dependencies of the real and imaginary parts of the aerosol refractive index and, therefore in the spectral dependence of SSA (Dubovik and King, 2000). Comparison of column SSA retrieved from the AERONET with in situ profile measurements revealed that the majority of SSA comparisons when AOD at 0.44 $\mu m >0.2$ were within the uncertainty bounds (Andrews et al., 2017). An intercomparison of SSA from AERONET and in situ aircraft profiles during the DRAGON-MD and DISCOVER-AQ experiments was found to be excellent, and further all the coincident measurement pairs were within the accuracies of the measurement techniques (Schafer et al., 2014).

In situ observations show that the aerosols can exist in different mixing states, usually a combination of the three idealized mixing states: external mixtures (when the different aerosol species such as sulfate, nitrate, organics, dust, BC, BrC, and sea salt, can co-exist without any physical or chemical interactions among themselves), core-shell mixtures (one aerosol species coats the other i.e., sulfate coats the BC particles or vice versa), and internal mixtures (all aerosol species are mixed together resulting in a single aerosol entity). Different types of aerosol mixing states have been observed in several in situ field observations comprising physical and chemical characteristics of aerosols, and they strongly vary with location and season (e.g., Zhang et al., 2003; Mallet et al., 2004; Arimoto et al., 2006; IPCC, 2013). The different aerosol mixing states can produce changes in aerosol size distribution, their life cycle and radiative effects. In AERONET retrievals the SSA and ARF are retrieved for columnar aerosols using direct and diffuse radiation measurements, i.e., direct and scattered radiation, and therefore the information on aerosol mixing is already embedded or accounted for while retrieving SSA and ARF. It should be noted that for both cases of internally and externally mixed particles, no significant errors were observed in the AERONET retrieval of SSA (Dubovik et al., 2000, 2006).

The AERONET measured solar fluxes were found to agree with ground-based measurements in all situations (urban-industrial, biomass burning, mineral dust, background continental, maritime aerosols and free troposphere) with a correlation higher than 99 % (García et al., 2008). Further, from an analysis of year-long data, the correlation between the model estimated radiative forcing (using AOD, SSA and asymmetry parameter measured by AERONET), and AERONET radiative forcing at the top of the atmosphere (TOA) and at the Earth's surface (SFC) was found to be very good (correlation coefficient ≥ 0.90) over an urban (Kanpur) and a rural (Gandhi College) location in the Indo-Gangetic Plain, and over an urban (Pretoria) site in South Africa (Ramachandran and Kedia, 2012; Adesina et al., 2014). To determine the impact of aerosols on climate the net gain/loss of energy at the surface and at the top of the atmosphere, and net energy trapped in the atmosphere (ATM) are more crucial than their respective variations as a function of altitude. Earlier studies have clearly shown that the inclusion of vertical profiles of aerosols did not significantly affect the net ARF at TOA, SFC, and ATM and the aerosol-induced atmospheric heating rate (Ramachandran and Kedia, 2012; IPCC, 2013), as the net energy content trapped in the atmosphere is found to remain the same in both the cases (with and without inclusion of aerosol vertical profiles). Sensitivity studies show that the degree to which the vertical profile of the aerosol distribution impacts the forcing depends on many factors such as the presence of clouds, SSA and surface albedo; when absorbing aerosols (with an SSA of 0.7–0.8) are present above or below clouds they may affect ARF at the top of the atmosphere (e.g., Choi and Chung, 2014). However, in the present study, the ARF retrieved for the clear-sky atmosphere available from AERONET at SFC and TOA are used. The ARF in the ATM is the difference between the two. The ARF at SFC is corrected for the effect of surface albedo by multiplying operational AERONET ARF

at SFC by $(1-SA)$, where SA is spectral average surface albedo. Since the objective of the study is to determine the net energy trapped in the atmosphere (expressed in terms of heating rate), non-inclusion of aerosol vertical profiles is not expected to modify any inferences or key results.

Atmospheric solar heating rate: The atmospheric solar heating rate due to aerosols (Kelvin day⁻¹) is obtained using the aerosol radiative forcing in the atmosphere (ARF_{ATM}) as,

$$\frac{\partial T}{\partial t} = \frac{g}{c_p} \times \frac{ARF_{ATM}}{\Delta P} \times 24(\text{hr/day}) \times 3600(\text{sec/hr})$$

where $\partial T/\partial t$ is the HR, g is the acceleration due to gravity (9.8 ms^{-2}), c_p is the specific heat capacity of air at constant pressure ($1006 \text{ J kg}^{-1} \text{ K}^{-1}$), and ΔP is the pressure difference between the elevation of observation site (Table 1) and 10,000 m asl.

The common procedure of computing the aerosol-induced atmospheric heating rate is to use the pressure difference between the surface (elevation of observation site in m asl) and 5000 m asl over the site, since generally most of the aerosol mass in the troposphere resides between the surface and 5000 m asl (IPCC, 2013; Ramanathan et al., 2007a). However, we use 10,000 m asl as the upper bound, since the primary objective of the study is to examine the radiative impact due to aerosols over the Himalayan-Tibetan Plateau region, which has mountain peaks extending up to ca. 9000 m asl.

3.2. Satellite data: MODIS, OMI and CERES

The Moderate Resolution Imaging Spectroradiometer (MODIS) AOD was calculated from the daily mean AOD (corresponding to $0.55 \mu\text{m}$) from MODIS Daily L3 Global 1° datasets acquired from the Level-1 and Atmosphere Archive and Distribution System (LAADS) (https://ladsweb.modaps.eosdis.nasa.gov/archive/allData/61/MOD08_D3/). The uncertainty in MODIS AOD is $\pm 0.05 \pm 0.15 \text{ AOD}$ (Levy et al., 2013).

The monthly data of Ozone Monitoring Instrument (OMI) (https://disc.gsfc.nasa.gov/datasets/OMAERO_003/summary) SSA created using the first 23 clean rows of OMI Level-2 product (out of total 60 rows) that are free of row anomaly (Torres et al., 2018) are utilized. The OMI SSA at $0.388 \mu\text{m}$ is used because retrievals at the other wavelengths in the OMAERUV dataset are not directly derived from the measurements, but converted from $0.388 \mu\text{m}$ retrievals assuming a spectral dependence model depending upon the chosen aerosol model. Due to a few inherent uncertainties in the assumed spectral dependence, which might not represent all aerosol types/conditions globally, it has been recommended to use the $0.388 \mu\text{m}$ SSA dataset (Torres et al., 2018). The OMI observations, since the middle of 2007, have been affected by a possible external obstruction that perturbs both the measured solar flux and Earth radiance. This obstruction, which affects the quality of radiance at all wavelengths for a particular viewing direction, is referred to as a “row anomaly” since the viewing geometry is associated with the row numbers on the charge-coupled device detectors (Torres et al., 2018). The row anomaly issue was detected initially for a few rows which, over the period of operation, expanded to other rows in 2008 and later. Currently, about half of the total 60 rows (viewing positions) across the track are identified and flagged as affected by row anomaly for which no physical retrievals are being performed. Due to the row anomaly issue and some scan-related bias in the OMI SSA retrievals (Torres et al., 2018), we have utilized the level-2 OMAERUV product for SSA derived using only the first 23 rows that are unaffected by the row anomaly throughout the OMI operation for comparison. SSA derived using viewing positions 1–30, and 31–60 were found to agree over regions dominated by carbonaceous or sulfate particles (Torres et al., 2018). The Level-2 retrievals are aggregated on to each $0.5^\circ \times 0.5^\circ$ grid. Note that only best quality retrievals (Quality Flag = 0) of SSA at $0.388 \mu\text{m}$ are included in this analysis.

The Clouds and the Earth's Radiant Energy System (CERES) measured Energy Balance and Filled (EBAF) data (edition 4.1, Loeb et al., 2018) monthly averages of daily shortwave clear-sky ARF are utilized. The ARF at the TOA (ARF_{TOA}) and at the surface (ARF_{SFC}) at a latitude-longitude

resolution of $1^\circ \times 1^\circ$ are calculated synergistically using MODIS Terra and Aqua AODs. The CERES Synoptic Radiative Fluxes product (SYN1deg, edition 4A) is used to derive the change in the aerosol radiative effect. The CERES SYN product provides estimate of the radiative fluxes at TOA and surface, with and without the presence of aerosols (Paulot et al., 2018). In the SYN product, the radiative transfer calculations are carried out using aerosol properties from the Model for Atmospheric Transport and Chemistry (MATCH), which is constrained by observations from MODIS and CERES. Two modes of available fluxes are used: pristine (clear, no aerosols) and clear sky (clear, with aerosols and cloud free skies) conditions at the surface and TOA. The ARF_{TOA} is estimated by differencing net clear-sky from net pristine-sky fluxes. The variability in the shortwave clear-sky outgoing radiation in the CERES EBAF data is assumed to be due to the changes in aerosols (Paulot et al., 2018 and references therein). The ARF_{atm} (atmospheric forcing) is estimated as the difference between ARF_{TOA} and ARF_{SFC} .

3.3. Model simulations

Specific CMIP6 experiments are designed to explore the climate change arising from the changes in aerosols, greenhouse gases, and natural forcings. In this study, simulation results obtained from the U.K. Earth System Model (UKESM1-0-LL) (at the latitude-longitude resolution of $1.875^\circ \times 1.25^\circ$) which participated in the AerChemMIP and CMIP (Collins et al., 2017) experiments in the Coupled Model Intercomparison Project Phase 6 (CMIP6) (Eyring et al., 2016) are used for the analysis. The “historical”, “piClim-control”, “piClim-aer”, and “piClim-BC” experiments are used for this study (Eyring et al., 2016). The piClim-aer and piClim-control experiments are used for estimating the aerosol radiative forcing. The piClim-control run simulates conditions fixed at pre-industrial levels. It includes climatological average sea-surface temperatures (SSTs) and sea-ice distributions, greenhouse gas concentrations, and near-term climate forcers (NTCFs) emissions at 1850 values. The piClim-aer provides the aerosols forcing experiment by using present-day (2014) emissions of aerosols and aerosol precursors but keeping all other boundary conditions fixed at pre-industrial levels (see RfMIP; <https://rfmip.leeds.ac.uk/rfmip-erf/>). The piClim-BC run uses present-day (2014) BC emissions but keeping all other forcings at pre-industrial levels. The “piClim” simulations provide a time-slice experiment of 30 years in total, and includes both direct and indirect radiative effects of aerosols. In the UKESM1 model, aerosol particles are activated into cloud droplets using the activation scheme of Abdul-Razzak and Ghan (2000). The details on aerosol schemes and parameterizations used in UKESM1 model are given in Mulcahy et al. (2020). The UKESM1 is one of the most process complete and interactive earth-system models (ESMs) available currently, especially with respect to aerosols (Mulcahy et al., 2020). The MODIS derived AODs (both seasonal and spatial) are captured well in UKESM1 model (Mulcahy et al., 2020). Further, the UKESM1 model was chosen because not only the outputs on changes in aerosol radiative forcing and temperature due to changes in emissions were available but also due to the fact that it was able to simulate reasonably well the observed trends in aerosol characteristics over Asia in the last 2-decades (Ramachandran et al., 2022).

3.4. Details of comparison with earlier studies

We have compared the results that are relevant, appropriate and available over the region covering South and East Asia, including the Indian Ocean, IGP and the Himalayas; however, there are similarities (columnar data retrieved from the same instrument (AERONET)) and differences (methodology used to estimate aerosol radiative forcing) between the present study and the earlier studies. The comparison also includes results obtained earlier over Kanpur and Kathmandu, two sites used in the current study. The earlier studies were based on limited sets of measurements made during a particular season and/or over a particular location. Vertical profile measurements of aerosol absorption and scattering coefficients in the 0–3 km altitude range, AERONET AOD and a Monte Carlo Aerosol-Cloud Radiation (MACR) model were used to derive aerosol heating rates

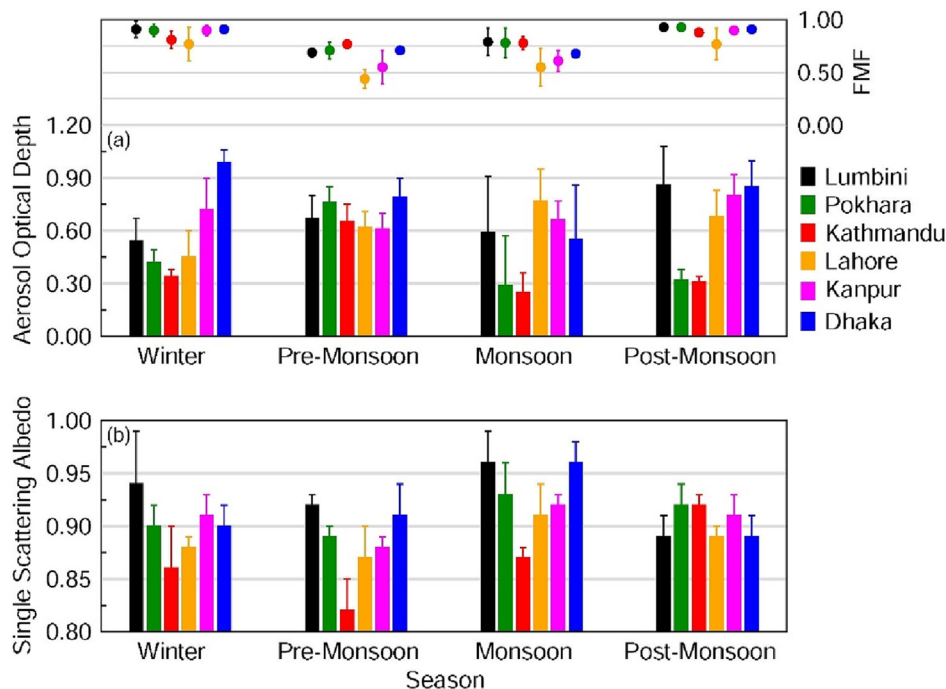


Fig. 4. Aerosol optical properties over the IGP and the Himalayan Foothills: (a) Seasonal mean aerosol optical depth (AOD), fine mode fraction (FMF) and (b) single scattering albedo (SSA) corresponding to a wavelength of $0.50 \mu\text{m}$. Vertical bars indicate $\pm 1\sigma$ (standard deviation) from the mean. Seasons are defined as winter: Dec–Feb; pre-monsoon: March–May; monsoon: June–September; and post-monsoon: October–November.

over the Maldives, though only during the pre-monsoon season (Ramanathan et al., 2007a); AOD and SSA, retrieved from MODIS, MISR and AERONET, along with MACR model results over the Maldives were used to derive ARF and ARFE, though only during the post-monsoon season (Ramanathan et al., 2007b), and AERONET retrieved AOD, SSA and asymmetry parameter over Kathmandu and Kanpur were used in a radiative transfer model to estimate ARF and ARFE (Cho et al., 2017). Our study, for the first time, documents the seasonal variation in ARFE derived from AERONET ARF and AOD over sites covering a large spatial domain that includes Pakistan, India, Nepal and Bangladesh, using year-round data.

4. Results and discussion

4.1. Aerosol optical depth and fine mode fraction

The significant seasonal and spatial variations of the aerosol optical depth (AOD), fine mode fraction (FMF) of AOD and single scattering albedo (SSA) over the IGP are seen in Fig. 4. Seasonal and annual mean (Fig. 4a, Table 2) AODs are all >0.3 across the IGP and the Himalayan foothills indicating that all sites are heavily polluted (Ramanathan et al., 2007b). The AOD over Lumbini (0.5–0.9) is significantly higher than the AODs over Pokhara and Kathmandu (0.3–0.6) in all seasons except the pre-monsoon, when it is marginally lower than Pokhara (Fig. 4a). Higher AODs at

elevated locations (Pokhara and Kathmandu) in the Himalayas during the pre-monsoon are influenced by the regional transport of aerosols from polluted continental and biomass burning regions of South Asia (especially the IGP) (Lüthi et al., 2015; Rupakheti et al., 2019; Singh et al., 2019; Ramachandran and Rupakheti, 2021). During monsoon the AODs are governed by local emissions, since precipitation suppresses the transport of regional emissions and also some major seasonal sources like brick production and forest fires are not active during the monsoon season. AODs over Lahore in the IGP are higher during the pre-monsoon and monsoon (Fig. 4) due to the dominance of coarse mode dust particles (which also results in lower FMF) compared to the other seasons. In contrast, AODs are higher over Kanpur during winter and the post-monsoon due to the dominance of fine mode aerosols. In Lumbini, AOD is the highest during winter when compared to the other seasons. AOD is >0.9 over Dhaka during winter (Fig. 4). The highest AOD throughout most of the year is over Dhaka (>0.8), with the relative reduction during monsoon being more pronounced here than at other locations. This is because Dhaka is close to the coast, and thus a greater amount of summer monsoon precipitation (1257 mm) leads to a more substantial reduction in aerosol content through wet removal compared to the precipitation at the other IGP locations (822 mm at Kanpur and 360 mm at Lahore).

Fine mode aerosols contribute $>70\%$ to the total AOD at all sites throughout the year, except for Lahore and Kanpur during the pre-monsoon and monsoon seasons (Fig. 4), confirming the dominance of fine

Table 2

Annual mean aerosol optical depth (AOD), fine mode fraction (FMF) of AOD, single scattering albedo (SSA), aerosol radiative forcing efficiency in the atmosphere (ARFE_{atm}), and aerosol-induced atmospheric solar heating rate along with $\pm 1\sigma$ (standard deviation) over the study locations derived from the AERONET observations (Fig. 1).

Location	AOD	FMF	SSA	ARFE_{atm} ($\text{Wm}^{-2} \text{AOD}^{-1}$)	Heating rate (K day^{-1})
1. Lumbini	0.67 ± 0.14	0.82 ± 0.12	0.93 ± 0.03	77.4 ± 39.8	0.54 ± 0.33
2. Pokhara	0.45 ± 0.22	0.81 ± 0.12	0.91 ± 0.02	93.4 ± 28.2	0.45 ± 0.32
3. Kathmandu	0.39 ± 0.18	0.80 ± 0.06	0.86 ± 0.04	132.5 ± 42.4	0.74 ± 0.45
4. Lahore	0.63 ± 0.13	0.61 ± 0.19	0.91 ± 0.02	84.3 ± 34.9	0.50 ± 0.27
5. Kanpur	0.70 ± 0.08	0.72 ± 0.19	0.92 ± 0.02	72.9 ± 25.5	0.48 ± 0.22
6. Dhaka	0.80 ± 0.18	0.79 ± 0.12	0.92 ± 0.03	85.0 ± 34.6	0.72 ± 0.35

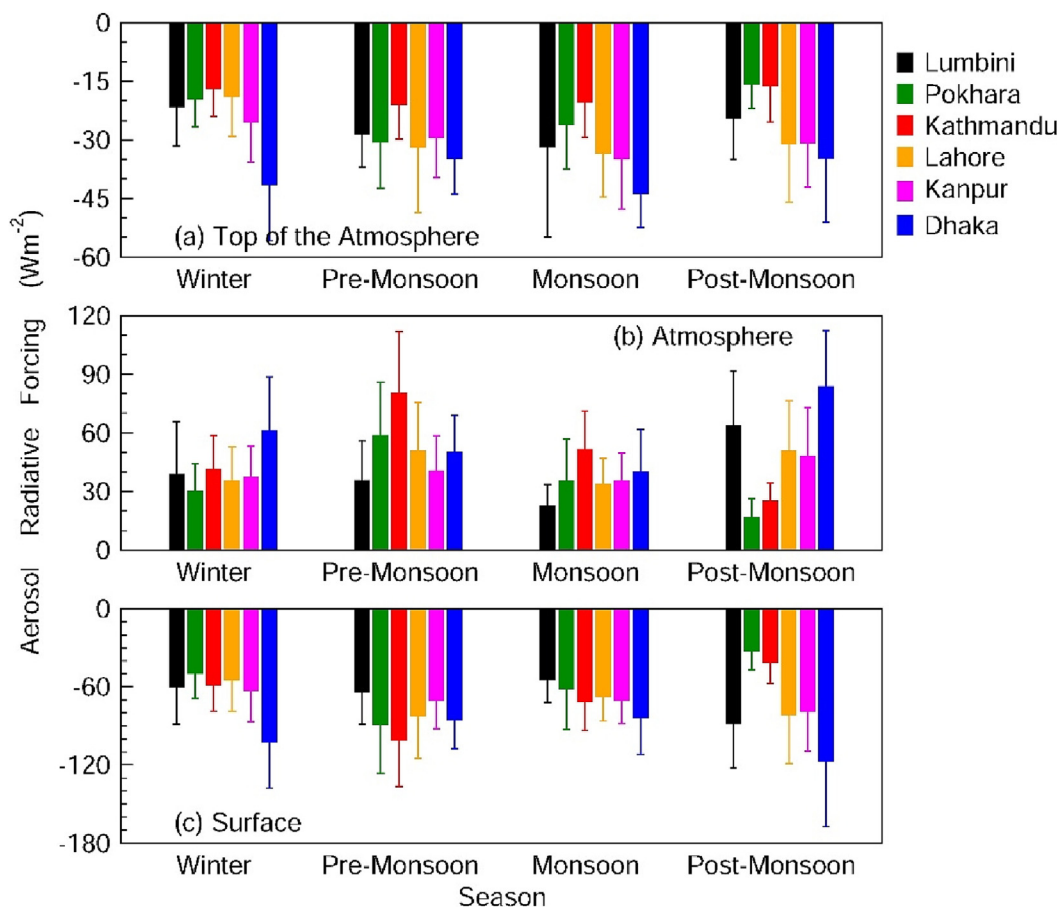


Fig. 5. Aerosol radiative forcing (Wm^{-2}) across seasons and locations in the IGP and Himalayan foothills: (a) at the top of the atmosphere, (b) in the atmosphere and (c) at the surface. Vertical bars correspond to $\pm 1\sigma$ (standard deviation) from the mean.

mode aerosols in the total AOD. A closer examination reveals that locations in the Himalayas have a relatively higher FMF (0.7–0.9) than the other locations in the IGP (0.4–0.9) as these sites are less (or not) influenced by dust or sea salt, while dust aerosols from nearby deserts affect Lahore and Kanpur and similarly sea salt affects Dhaka since it is near the Bay of Bengal. During the pre-monsoon season, Kathmandu has the highest FMF (0.8), due to local emissions and regional fine mode aerosol emissions from biomass burning. This includes agro-residue burning and forest fires in the upwind regions, which can reach altitudes higher than 2000 m asl in this region due to strong westerly winds (Rupakheti et al., 2019; Singh et al., 2019; Mahapatra et al., 2019), boundary layer dynamics in the region (Putero et al., 2018) and orographic lifting by the mountain-valley effect (Weissmann et al., 2005; Putero et al., 2018), thereby giving rise to a higher FMF at the elevated sites than the lowland sites. High FMF values over Pokhara and Kathmandu confirm the abundance of fine mode aerosols even at higher elevations in the Himalayan foothills. FMF in Lahore is the lowest throughout the year among all the locations due to the prevalence of coarse dust particles, and is particularly low during the pre-monsoon and monsoon periods due to the increase in the abundance of dust advected from nearby desert regions, as well as the contribution from sea salt particles and the hygroscopic growth of water soluble aerosols (e.g., sulfate) because of the high relative humidity during monsoon. A similar pattern is reflected in the FMF values for Kanpur and Dhaka, though with generally higher FMF values than Lahore.

4.2. Single scattering albedo

The SSA is a measure of the fraction of incoming solar radiation scattered by the particles in the atmospheric column. A lower SSA indicates

greater aerosol absorption, and vice versa. Kathmandu has the lowest annual mean SSA among all sites (Fig. 4b). Given that the AOD over Kathmandu is similar to the AOD in other regions, the lower SSA here suggests a larger contribution from absorbing aerosols present in the column over Kathmandu. Seasonally, the SSA over Kathmandu is <0.90 in the winter, pre-monsoon and monsoon, while it is slightly higher than 0.90 during the post-monsoon period, which confirms the abundance of light-absorbing carbonaceous aerosols (BC, and brown carbon (BrC)) over Kathmandu throughout the year, consistent with earlier results from surface (for winter) and columnar observations over Kathmandu (Cho et al., 2017; Ramachandran et al., 2020b). The BC and BrC aerosols arise largely from polluted continental and biomass burning emissions which get transported to higher elevations in the Himalayan region (Koch et al., 2009; Li et al., 2016; Xu et al., 2016; Gautam et al., 2011; Singh et al., 2019; Ramachandran and Rupakheti, 2021). Since BC has the strongest light-absorbing character (BC SSA = 0.19, BrC SSA = 0.85, and dust SSA = 0.84 at 0.55 μm) (Hess et al., 1998; Magi, 2011; Ramachandran et al., 2020b), the lower values of SSA can only occur through a dominance of BC in light-absorption, which has been reported for the IGP and Himalayan foothills regions in earlier studies (Gautam et al., 2011; Rupakheti et al., 2019; Ramachandran et al., 2020b). Low SSA values (0.86–0.89) were also reported previously for Nepal at even higher altitudes in the Himalayas (Dhulikhel (27.61°N, 85.53°E, 1500 m asl) and Langtang (28.01°N, 85.49°E, 3670 m asl)), based on limited observations during the pre-monsoon period in 2009 (Gautam et al., 2011), similarly confirming the dominance of BC in reducing SSA at higher altitudes in the Himalayas and foothills. An evaluation of aerosol type revealed that over all the locations in Nepal the aerosols were primarily of urban/industrial and biomass burning types whereas dust, as classified by the technique used in earlier studies (e.g., Rupakheti

et al., 2019), was nearly absent as an absorbing aerosol type over Lumbini, Pokhara and Kathmandu. BC was dominantly responsible for aerosol absorption throughout the year over the Himalayan region (Ramachandran et al., 2020b). In contrast, dust also played a considerable role over Lahore and Kanpur in the IGP, and the absorbing aerosols over the IGP were mostly BC, and BC mixed with dust. It is interesting to note that Kathmandu, despite being located at a higher elevation, has a lower SSA than Lumbini and Pokhara. This finding confirms that not only the fine mode particles are higher at higher altitudes in the central Himalayan foothills (e.g., Kathmandu, Pokhara) (Fig. 4a), but they are also more absorbing in nature (more BC) (Fig. 4b), giving rise to lower SSA values than over the IGP sites. This result is strengthened by the finding that fossil fuel combustion and biomass burning contribute almost equally to elemental carbon (EC, chemical/mass definition of BC) in South Asia (Gustafsson et al., 2009) and the Himalayan region (Li et al., 2016) whereas the share of fossil fuel combustion is ca. 80 % in East Asia (Li et al., 2016), and that the mass absorption cross-section of EC (MAC_{EC}) generally increases with increasing altitudes in the HTP region (Li et al., 2016; Chen et al., 2019).

4.3. Aerosol radiative forcing and efficiency from observations and model simulations

The seasonal average aerosol radiative forcing at the surface (ARF_{sfc}) over the study region exceeds -50 Wm^{-2} throughout the year (Fig. 5). The aerosol radiative forcing efficiency (ARFE) (Fig. 6), which is the ARF normalized to the AOD (shown earlier in Fig. 4a), is a useful measure to quantify the influence of aerosol absorption and scattering (as a further indicator beyond the SSA). ARFE indicates the rate at which the atmosphere is forced radiatively per unit of AOD, thereby filtering out the influence of aerosol loading (AOD) on ARF. ARFE at the top of the atmosphere ($ARFE_{toa}$)

shows less significant seasonal and spatial variations than ARFE in the atmosphere ($ARFE_{atm}$) and at the surface ($ARFE_{sfc}$). ARFE values obtained from observations over the Himalayas (Fig. 6) are at least 2–4 times higher than those obtained in previous studies over the regions surrounding the Himalayas, for example over the northern Indian Ocean (Ramanathan et al., 2007b), and East Asia - Beijing (China) and Gosan (S. Korea) (Cho et al., 2017) owing to higher AOD (>0.30), and aerosol absorption ($SSA < 0.95$) (Fig. 4). Models grossly underestimate ARFE over South Asia and East Asia (Cho et al., 2017). For the Nepalese sites, the magnitudes of $ARFE_{sfc}$ and $ARFE_{atm}$ increase with altitude, with the highest values at Kathmandu (Fig. 6). The difference in $ARFE_{sfc}$ and $ARFE_{atm}$ between Lumbini and Kathmandu, separated in elevation by ca. 1 km, is at least $>50 \text{ Wm}^{-2} \text{ AOD}^{-1}$ throughout the year, exceeding 100 Wm^{-2} during the winter and the pre-monsoon periods (Fig. 6). Although the annual mean $ARFE_{sfc}$ and $ARFE_{atm}$ are the highest for Kathmandu among the study locations, the variation ($\pm 1\sigma$ standard deviation) there is relatively low, with the $ARFE_{atm}$ value of Kathmandu remaining consistently $>130 \text{ Wm}^{-2} \text{ AOD}^{-1}$ throughout the year (Table 2). $ARFE_{sfc}$ and $ARFE_{atm}$ (ARF_{sfc} and ARF_{atm} as well (Fig. 5)) roughly follow the inverse of the SSA (Fig. 4b), since a higher fraction of absorbing aerosols (lower SSA) results in a greater radiative efficiency of aerosols for the same aerosol radiative forcing value (e.g., Ramanathan et al., 2007b).

The ARF simulated by UKESM1 model in the CMIP6 is significantly lower than the observations over Asia, since the simulated AOD is lower, and the SSA is higher than observations (Fig. 7), so that the simulated ARF (Fig. 8) and ARFE (Fig. 9) are lower than in the observations. In stark contrast to the observations (Fig. 4), simulated AOD is <0.3 over the HKHTP region throughout the year and SSA is in the 0.85–0.92 range, being higher than 0.9 in the HKHTP mountain region (Fig. 7). ARFE values from model (Fig. 9) and satellite observations (Fig. 10) are at least a factor

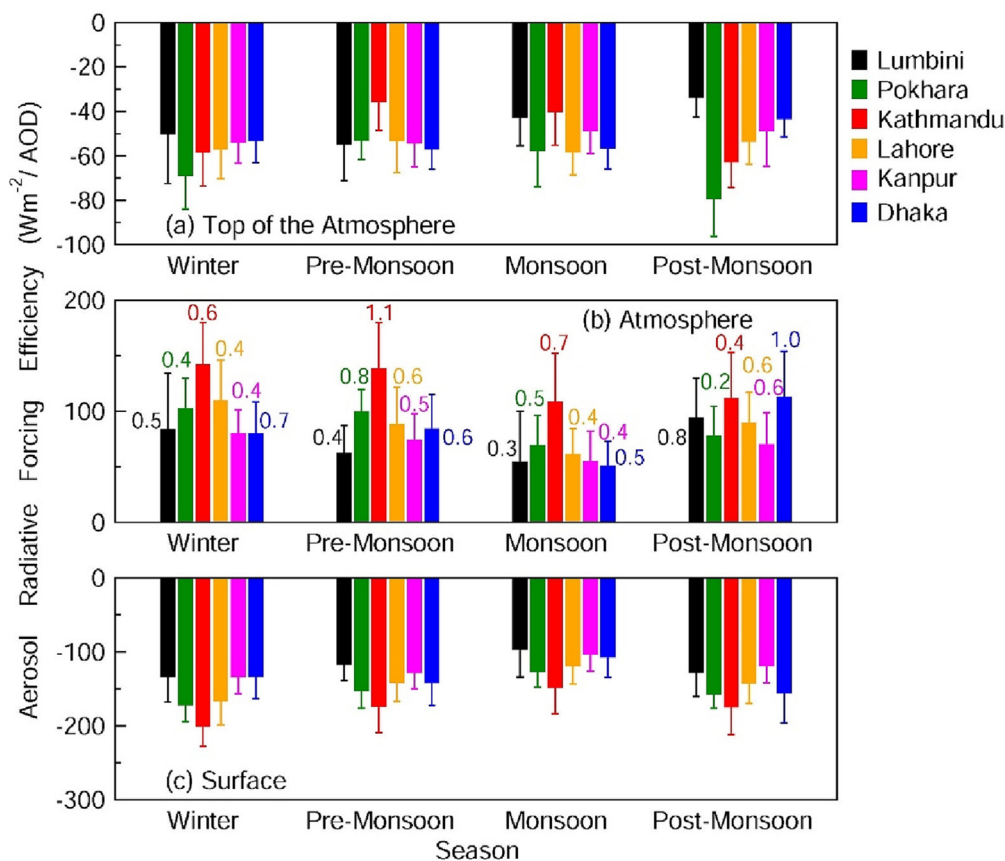


Fig. 6. Aerosol radiative forcing efficiency (Wm^{-2} per unit AOD) across seasons and locations in the IGP and Himalayan foothills: (a) at the top of the atmosphere, (b) in the atmosphere and (c) at the surface. Vertical bars represent $\pm 1\sigma$ (standard deviation) from the mean. The seasonal mean atmospheric solar heating rate (Kelvin day^{-1}) estimated using the aerosol radiative forcing (Wm^{-2}) in the atmosphere corresponding to each location for each season is given as values above the bars in (b).

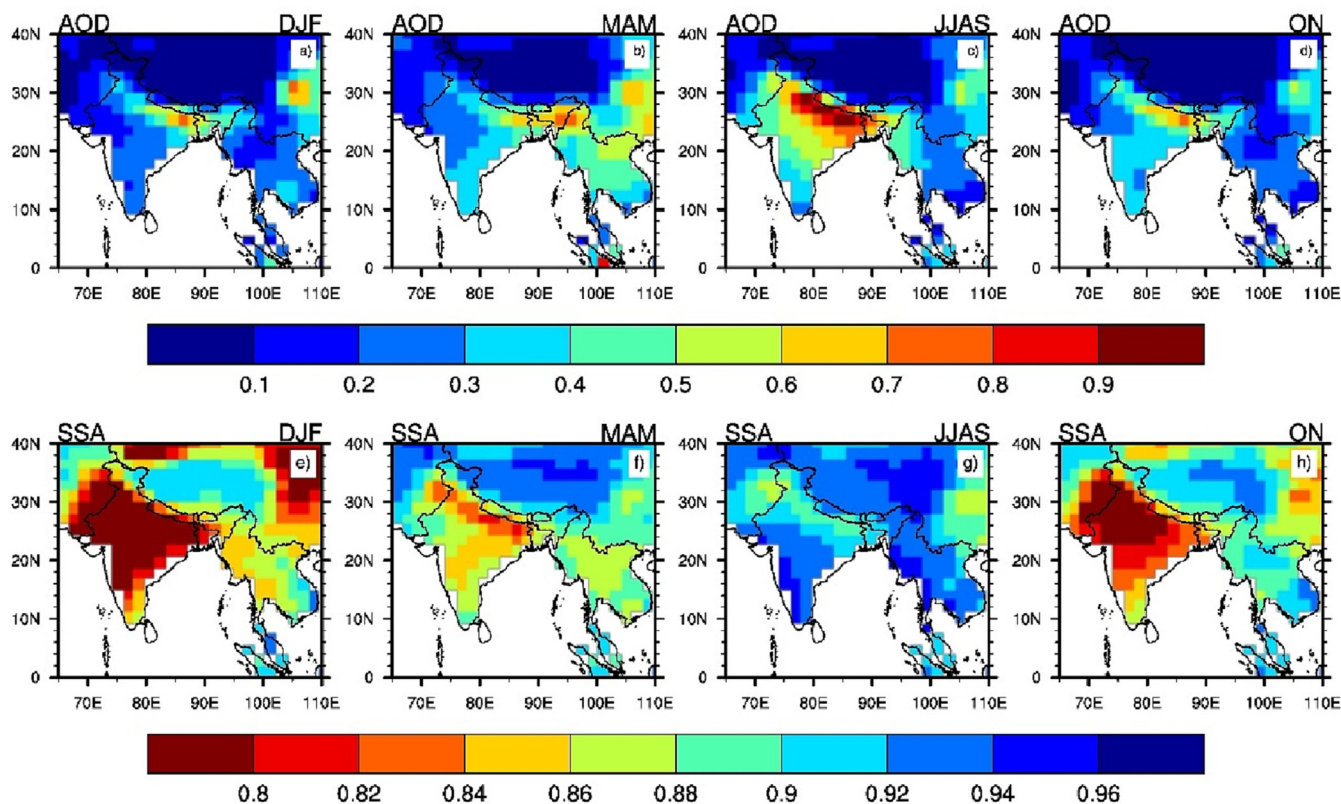


Fig. 7. Seasonal average aerosol characteristics simulated by UKESM1 model over South Asia for the year 2014: aerosol optical depth (AOD) in (a) winter (DJF), (b) pre-monsoon (MAM), (c) monsoon (JJAS), (d) post-monsoon (ON), and single scattering albedo (SSA) in (e) winter, (f) pre-monsoon, (g) monsoon, and (h) post-monsoon.

of 2–4 lower than in our analysis of ground-based observations across the study region (Fig. 6). The higher in situ observed ARFE values are accompanied by higher AOD values, which means that the difference is due to much lower observed than simulated SSA values. MODIS AODs across the IGP are significantly lower over the HKHTP region (Fig. 2) when compared to ground-based observations. The differences between ground-based and satellite AODs, and ground-based observations and model simulations on a seasonal scale are of the order of 20–50 % over the IGP and the HKHTP region (Figs. 2, 4, 7). The strong seasonal signature seen in SSA from ground-based observations is missing in the satellite (OMI) observations as well as in model simulations (Figs. 2, 4, 7). Sampling differences, assumptions made during the satellite retrievals of aerosol products in the algorithms, missing information on particle properties and state of mixing of aerosol species, and cloud screening, along with uncertainties while deriving AOD, SSA and absorption AOD can give rise to differences between satellite and ground-based measurements (Ramachandran et al., 2015). Further, satellite retrieval of aerosol absorption, the key for an accurate estimate of SSA, is more challenging over bright surfaces, especially in the HKHTP region, and is therefore frequently unreliable and exhibits substantial biases (Shindell et al., 2013). The models are found to underestimate aerosol absorption especially over South Asia at least by a factor of 2–5 (Shindell et al., 2013; Ramachandran et al., 2021). Even over high-altitude regions, which are not aerosol source regions, BC emissions and absorption were grossly underestimated by models (Koch et al., 2009; Ramachandran et al., 2015; Ramachandran et al., 2021). The underestimation of BC was attributed to the lack of proper inventories of aerosol emissions, especially the region-specific fossil fuel combustion and biomass burning emissions (Shindell et al., 2013; Ramachandran et al., 2015; Quennehen et al., 2016; Ramachandran et al., 2021; Ansari and Ramachandran, 2023). The underestimation of BC in emission inventories also arise due to under-characterized sources (such as garbage burning and forest fires in South Asia), and missing BC source categories such as kerosene

emissions, used in lamps for lighting (Lam et al., 2012; Klimont et al., 2017).

Recent studies have shown that the sites in the Himalayas, remote parts of the Tibetan Plateau and the IGP are heavily affected by regional emissions (Singh et al., 2019; Mahapatra et al., 2019; Lüthi et al., 2015; Li et al., 2016). Therefore, the local emission inventory of various aerosol species and/or their precursors may not necessarily capture the columnar-aerosol characteristics, especially in a region like the HTP mountain regions, which are affected heavily by regional pollution. In order to apportion the contributions of local and regional emissions of light-absorbing aerosols to the observed AOD and SSA over these sites, new improved emission inventories (including BrC, and missing emissions (e.g., kerosene use) which are not included in most current inventories) would be needed, along with atmospheric simulations with regional chemistry transport models. This is crucial over a region where not only the aerosol types are different but also their emissions occur from diverse anthropogenic and natural sources ranging from cooking stoves to garbage burning to transportation, among others. It is quite a challenge to simulate aerosol characteristics more accurately over this region with distinct and complex variations in terrain, elevation and meteorological conditions. In addition, the uniqueness of aerosol characteristics over the HKHTP region because of this region being in close proximity to global aerosol hotspot and heavy influence of biomass burning among others makes it more challenging as this region is influenced by both local and regional emissions, which contribute to the aerosol population in almost equal proportions as opposed to several high-altitude sites which are at least partly in the free troposphere over which the local/surface level aerosol contribution will be less and where the aerosols from long-range transport dominate. Interestingly, the missing strong aerosol forcing signals can also depend on the formulation of individual models, and internal variability in the models. In addition, the simulated regional aerosol signals have different sensitivity to small perturbations in the initial conditions in different models

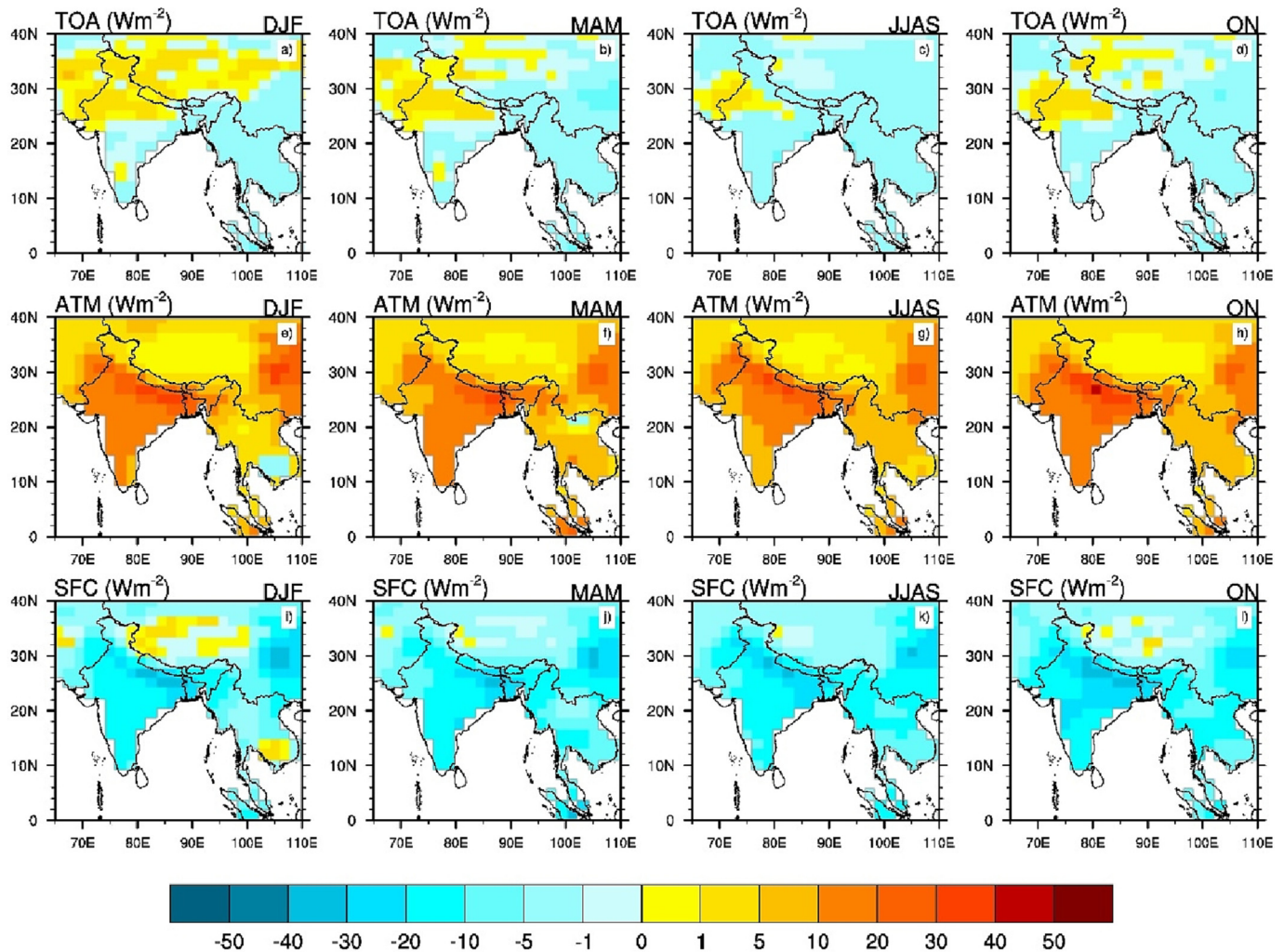


Fig. 8. Aerosol radiative forcing (Wm^{-2}) over the IGP and the Himalayas simulated by the UKESM1 model in CMIP6 simulations: at the top of the atmosphere (TOA) ((a) winter, (b) pre-monsoon, (c) monsoon, (d) post-monsoon), in the atmosphere (ATM) ((e) winter, (f) pre-monsoon, (g) monsoon, (h) post-monsoon)), and at the surface (SFC) ((i) winter, (j) pre-monsoon, (k) monsoon, (l) post-monsoon).

(Salzmann et al., 2014). However, these signals may be averaged out in global climate models, especially in elevated locations. Therefore, this study emphasizes the need for high-resolution regional models with updated emission inventories to address the aerosol impacts, especially over the high altitude locations. Thus, not only local aerosol emissions but also the transport from source regions that bring in the aerosols, along with their transformation and removal mechanisms over the HTP region need to be more accurately simulated (Lawrence and Lelieveld, 2010) to devise the necessary climate change and air pollution mitigation measures.

4.4. Atmospheric warming and cooling by aerosols

The atmospheric solar heating rate (Table 2) is high ($0.5\text{--}0.8 \text{ K day}^{-1}$) for all sites considered in this study, again being the highest for Kathmandu. The pre-monsoon heating rate of $\geq 1 \text{ K day}^{-1}$ over Pokhara and Kathmandu (Fig. 6b) is at least 1.5-times higher than previously reported values in the range of $0.45\text{--}0.7 \text{ K day}^{-1}$ due to BC in so-called “atmospheric brown clouds” (ABCs) between 500 and 3000 m asl during March 2006 over the Indian Ocean (Ramanathan et al., 2007a). Results obtained using the same columnar aerosol parameters retrieved from the same instrument (AERONET) in all sites are only being compared here (see Section 3.4 “Details of comparison with earlier studies”) for the sake of completeness and uniformity. Higher observed ARFE_{atm} and heating rate values on a regional scale in different seasons obtained in the current study when compared to

earlier studies (Ramanathan et al., 2007a, 2007b; Xu et al., 2016; Cho et al., 2017) indicate that earlier values do not appropriately portray the regional picture. Further, in recent global climate model simulations with an observationally-constrained BC aerosol forcing, BC aerosols produced a radiative heating rate that was significantly lower than our observations (Fig. 6), and BC warming over the Tibetan Plateau was almost equal to that of CO_2 (Xu et al., 2016). BC dominates (>75 %) the aerosol absorption throughout the year (Ramachandran et al., 2020b), and thus contributes almost the entire aerosol-induced warming in the lower atmosphere over the IGP and the HTP. The UKESM1 model CMIP6 simulations show that on an annual basis, BC aerosols contribute >50 % of the total warming (aerosols and GHGs combined) in the 3–5 km altitude region (Figs. 11, 12, 15). This is consistent with previously reported model-simulated annual warming of about 0.6 K at 3000 m asl over the HTP region for the period 1950–2000 due to aerosols in the ABCs, which accounted for half of the total lower atmospheric warming (Ramanathan et al., 2007a). The Community Climate System Model version 3 (CCSM3) simulations also showed that the BC aerosols act to increase the lower tropospheric heating over South Asia and reduce the amount of solar radiation reaching the surface (Meehl et al., 2008), as seen in the present study.

The UKESM1 simulates a significantly lower warming ($\sim 0.2 \text{ K}$) of the lower atmosphere due to aerosols over the IGP and the HTP region (Fig. 12). Over the HTP region the all-aerosol forcing produces a cooling of $\sim 0.2 \text{ K}$ or more in the lower atmosphere (Fig. 13, mainly due to sulfate

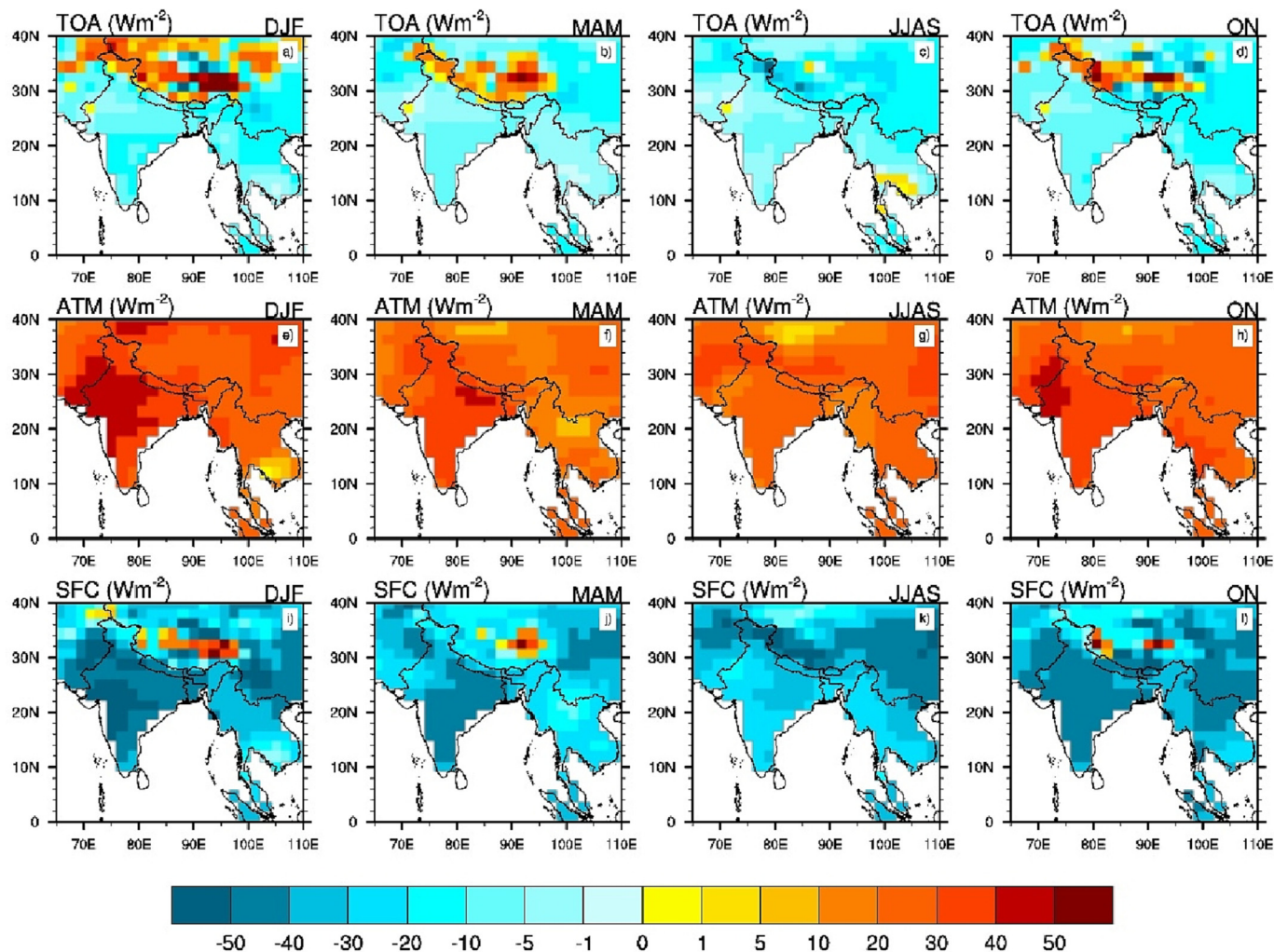


Fig. 9. Aerosol radiative forcing efficiency (Wm^{-2} per unit AOD) across the Himalayas simulated by UKESM1 model in the CMIP6: at the top of the atmosphere (TOA) ((a) winter, (b) pre-monsoon, (c) monsoon, (d) post-monsoon), in the atmosphere (ATM) ((e) winter, (f) pre-monsoon, (g) monsoon, (h) post-monsoon), and at the surface (SFC) ((i) winter, (j) pre-monsoon, (k) monsoon, (l) post-monsoon)).

aerosols (Figs. 14, 15) during the pre-monsoon and monsoon periods. The model-simulated warming/cooling by aerosols in the atmosphere shows significant seasonal variability. The aerosol cooling effect dominates during the monsoon whereas during the post-monsoon period the warming is dominant. Further, across India a north-south gradient in aerosol warming is seen; during winter at 500 hPa the aerosols cause a warming over northern India whereas a cooling over peninsular and southern India. Over the IGP region a warming of about 0.2°K is visible in the all-aerosol forcing simulations during post-monsoon and winter. During the year the arid/semi-arid regions adjacent to India are warmed by aerosols. Furthermore, the warming/cooling pattern exhibits an altitudinal gradient; the magnitude increases as the altitude increases from 3000 to 5500 m asl. A cooling of the lower atmosphere (e.g., during the pre-monsoon) is a clear indication of dominance of scattering aerosols (e.g., sulfate, organics) in the column producing a higher SSA (Fig. 7) which results in cooling. SSA is >0.92 over the HTP region throughout the year (Fig. 7) in model simulation. A lack of warming in the lower atmosphere due to aerosols in simulations confirms a significant underestimation of absorbing aerosols (especially BC) in the column in the UKESM1 model, and an overestimation of scattering aerosols which will mask the warming produced by absorbing aerosols significantly. Thus, it is clear that the current state-of-the-art climate models (e.g., UKESM1) involved in CMIP6 (which were used in the IPCC AR6) underestimate the atmospheric warming due to aerosols over the HTP region in the lower atmosphere. This is confirmed by the recent

study (Kelesidis et al., 2022) where it was shown that global climate models underpredict ARF due to BC aerosols largely due to the assumed morphology of BC. It was shown that light-absorption by BC aerosols enhanced due to morphological changes and the resultant aerosol absorption agreed well with AERONET observed BC absorption. The simulations further emphasized that accounting for realistic BC morphology resulted in higher ARF over South Asia which agreed with satellite and AERONET observations of ARF as reported in Ramachandran and Rupakheti (2020). Further, the simulations indicated that BC aerosols alone could be contributing a regional climate warming of about 1°C in the region (Kelesidis et al., 2022) which is consistent with our findings.

These features and magnitudes of warming/cooling due to aerosols in the present study are different from previous model results (e.g., Ramanathan et al., 2007a) in several ways. The past simulations were conducted with coupled ocean-atmosphere NCAR CCM3 model and took into account only the direct radiative effects of sulfate aerosols (Ramanathan et al., 2007a). Further, the ABC-induced temperature changes using the CCM3 model were estimated as the difference between the simulations imposed with and without the 2000–2003 forcing. Their study also used the emission data for aerosol precursors such as for SO_2 and soot (BC) from 1930 to 2002 and scaled the forcing with published data for soot and SO_2 emission rates as a function of time to derive a time dependent forcing from 1930 to 2000 (Ramanathan et al., 2007a). It was stated that the weakness of the study is that it cannot account for potential

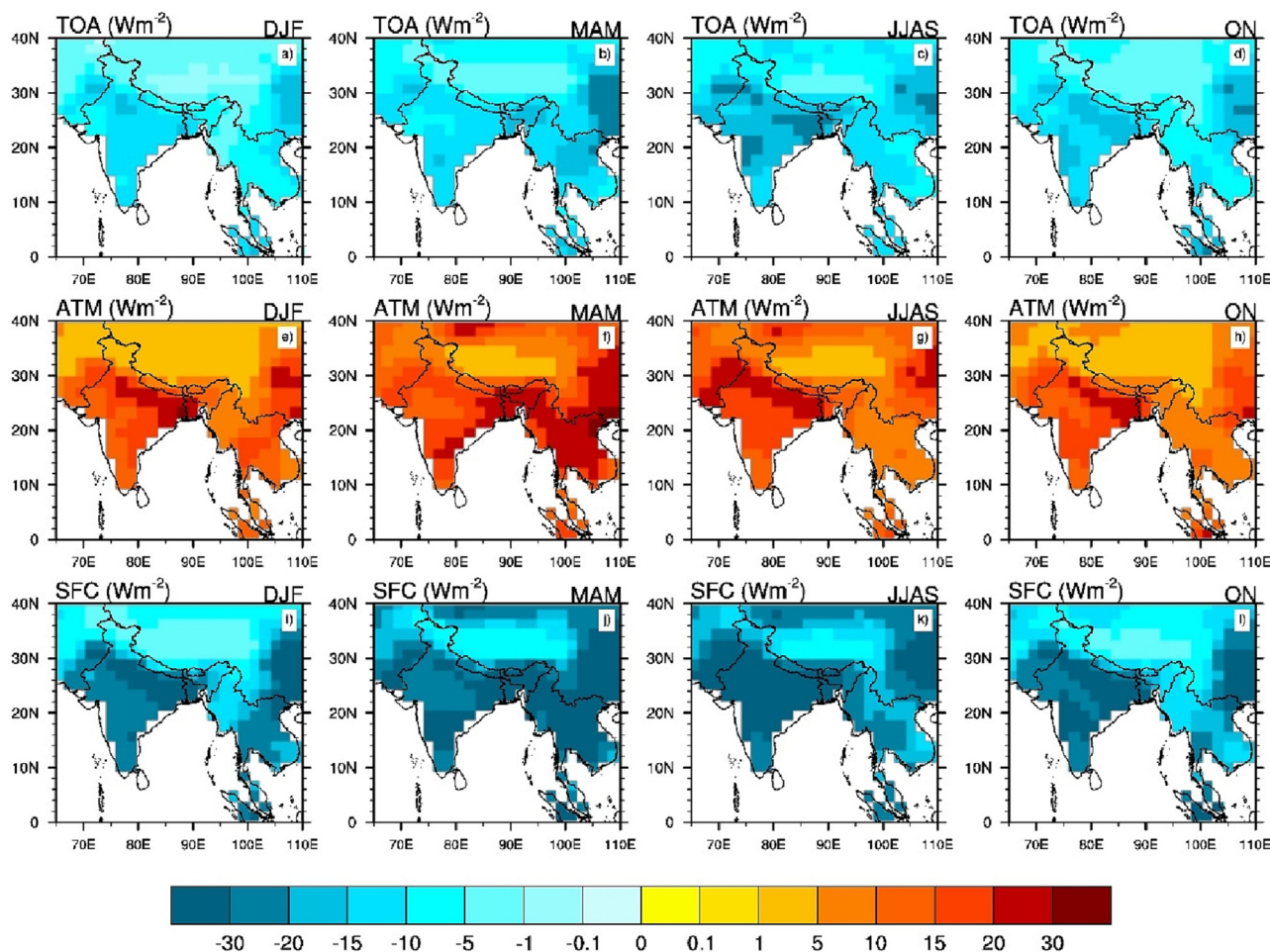


Fig. 10. CERES Satellite derived aerosol radiative forcing (Wm^{-2}) over the IGP and the Himalayas: at the top of the atmosphere (TOA) ((a) winter, (b) pre-monsoon, (c) monsoon, (d) post-monsoon)), in the atmosphere (ATM) ((e) winter, (f) pre-monsoon, (g) monsoon, (h) post-monsoon)) and at the surface (SFC) ((i) winter, (j) pre-monsoon, (k) monsoon, (l) post-monsoon)).

feedbacks between the forcing and the response, for example the changes in circulation as a result of forcing altering the aerosol concentrations (Ramanathan et al., 2007a). In contrast, in the present study, the warming due to aerosols correspond to the changes that occurred in the year 2014 with respect to the year 1850, similar to IPCC assessments, and includes both direct and indirect radiative effects of aerosols. The results in the current study also differ in terms of estimating the warming/cooling due to aerosols, as ARF is estimated from the simulated aerosol characteristics by the models, whereas the other studies including the aforementioned study (Ramanathan et al., 2007a) prescribed the ARF.

The other light-absorbing carbonaceous aerosol - brown carbon (BrC) is receiving more attention recently. However, BrC absorption is strongly wavelength dependent (the absorption is significantly less than BC, effective only over a narrow wavelength band in the 0.3 to 0.6 μm wavelength range, and falls very sharply above 0.4 μm), and thus it does not make a significant contribution to total light absorption beyond 0.55 μm (<5% over the Himalayan region) (Kirillova et al., 2016). As BC is five times more strongly absorbing than BrC, and it is the dominant light-absorber compared to dust and BrC over the IGP and the Himalayan foothills (Ramachandran et al., 2020b), the atmospheric heating by BC is likely to be a major climate-forcer in the Himalayan region. Our study, based on observations, reveals that in the present-day situation, the contribution of aerosol-induced heating to the total atmospheric warming could be even >50%. This difference is because the observed aerosol heating rates (Fig. 6, Table 2) are significantly higher than previously reported (e.g., in Ramanathan et al., 2007a) throughout the year over a large region covering

Pakistan, India, Nepal and Bangladesh, with the peak occurring during the pre-monsoon period at higher elevations.

Beyond the sites analyzed here, there are also three high altitude AERONET sites, at QMOS-CAS near Mt. Everest (28.36°N, 86.95°E, 4276 m asl) and Nam Co (30.77°N, 90.96°E, 4746 m asl) on the Tibetan Plateau (China), and Ev-K²-CNR (27.95°N, 86.82°E, 5079 m asl) near the base-camp of Mt. Everest (Nepal) (Fig. 1). No inversion data products are available for the Ev-K²-CNR site. Furthermore, as the data from QMOS-CAS and Nam Co are available only for a few days during 2012–15, we have not included the data from these locations in the study. The limited measurements, however, provide evidence that the ARFE_{sfc} and ARFE_{atm} over Nam Co was ca. $100 \text{ Wm}^{-2} \text{ AOD}^{-1}$ higher than over Kathmandu, and although the annual mean aerosol atmospheric heating rate is lower ($0.4 \pm 0.1 \text{ K day}^{-1}$), it is quite high for this altitude. This clearly indicates that as the elevation increases in the HTP region, ARFE_{atm} also increases. These results call for more measurements like these, especially in the HTP region – although they are quite challenging at higher elevations – to document more robustly the effects of aerosols on climate change in the region.

4.5. Implications

Such high ARFE and aerosol heating rate values observed over the Himalayas have significant implications for the climate (Xu et al., 2016) and hydrological cycle. The near surface air temperature trend over the Himalayas during the past decades has increased to between 0.2 and

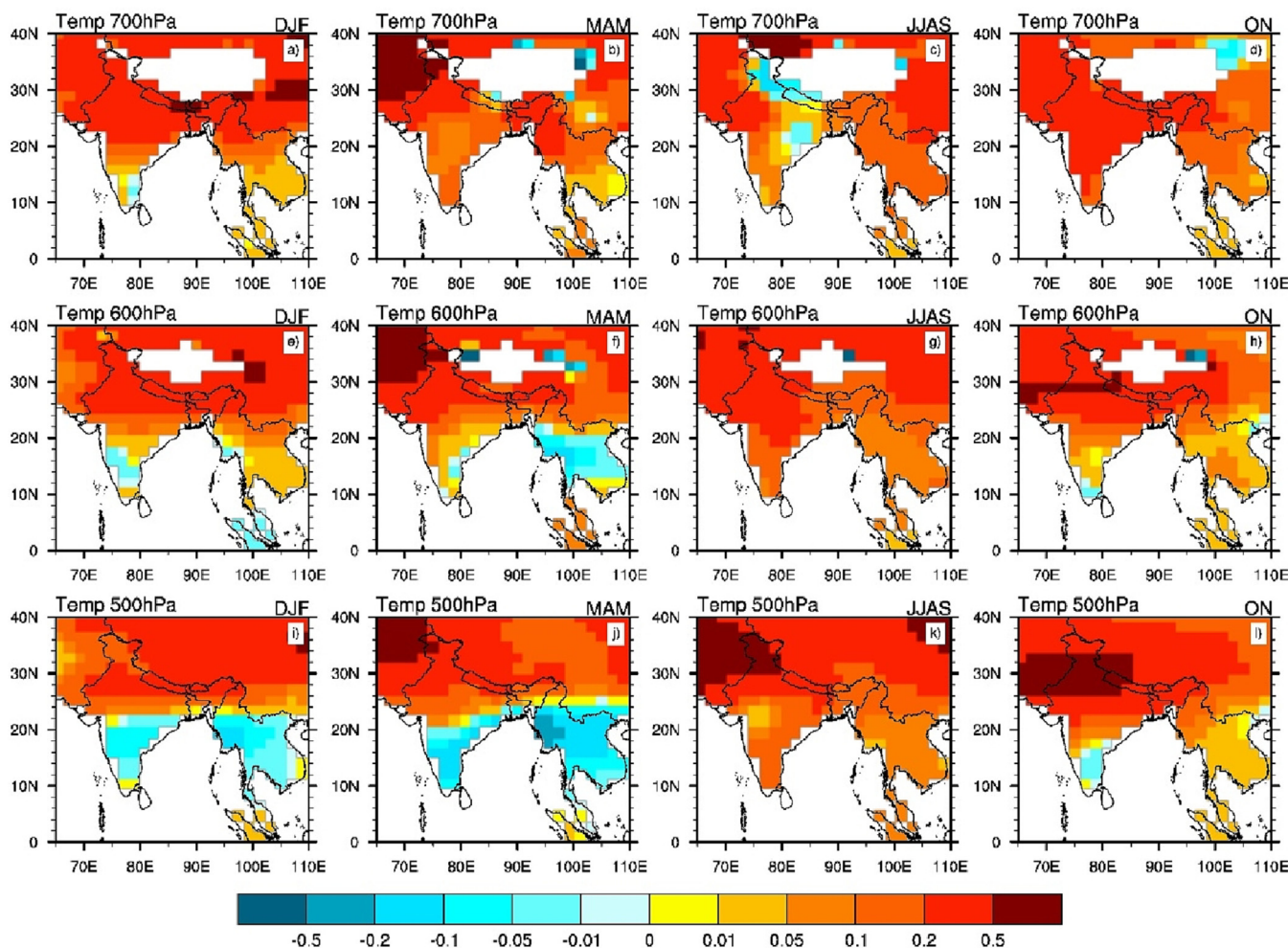


Fig. 11. The change in temperature (K) due to BC aerosols at three altitudes across the IGP and the Himalayas simulated by UKESM1 model. The change in temperature corresponds to year 2014 with respect to 1850. Temperature change during winter ((a) 700 hPa (~3000 m), (e) 600 hPa (~4250 m) and (i) 500 hPa (~5500 m)), pre-monsoon ((b) 700 hPa, (f) 600 hPa and (j) 500 hPa), monsoon ((c) 700 hPa, (g) 600 hPa and (k) 500 hPa), and post-monsoon ((d) 700 hPa, (h) 600 hPa and (l) 500 hPa). The white-shaded regions denote the part of the Himalayas with surface pressure <600 hPa or whose surface elevations are higher than about 4250 m asl.

0.3 °C per decade since the mid-1950s, significantly higher than the global average temperature increase (Liu and Chen, 2000; Krishnan et al., 2019). In addition, there is a tendency for the warming rate to increase at higher elevations in the Tibetan Plateau and its surrounding regions (Liu and Chen, 2000; Krishnan et al., 2019) as seen here for the case of aerosol-induced atmospheric warming. The atmospheric warming due to aerosols can alter regional atmospheric stability and vertical motions, affect large-scale circulation and the hydrological cycle, and thus be accompanied with significant regional climate effects and consequent impacts (Menon et al., 2002). The HKHTP region, which contains the largest ice mass outside the Antarctic and Arctic polar regions, has witnessed a pronounced retreat in the glaciers (Thompson, 2003; Sharma et al., 2019) that feed into the Yangtze, the Indus and the Ganges, the major rivers in Asia. The major cause for the HTP glacier ablation is attributed to this amplification of regional temperature increase (Liu and Chen, 2000). The aerosol-induced atmospheric warming and deposition of light-absorbing carbonaceous aerosols on snow and ice are expected to accelerate glacier and snow melt (Xu et al., 2016; Ramanathan et al., 2007a; Ramachandran et al., 2020b). Our findings corroborate a recent study (Maurer et al., 2019) which suggested that the consistent ice loss observed along the entire 2000-km transect of the Himalayas could dominantly be due to a regionally coherent climate forcing as a result of direct heating of the atmosphere by absorbing aerosols. The rapid retreat of glaciers is expected to negatively affect the water supply in southern and eastern Asia, with significant consequences for the regional hydrological cycle (Barnett et al., 2005). Given

that air pollution upwind of the HTP region is likely to remain a major challenge as a global air pollution hotspot in the decades to come (Kumar et al., 2018), we expect that the ARF will remain a key factor that drives climate change over the HTP region. It is amply clear from the comprehensive analysis here using ground-based and satellite observations along with model simulations that satellites and models still significantly underestimate (by a factor of 2 to 4) the aerosol-induced atmospheric heating and warming over this region. These new results need to be taken into account while examining the projected/expected present and future climate impacts due to aerosols, and the potential value of various mitigation measures, in particular on regional and decadal climate change in Asia. The higher atmospheric heating rate due to aerosol-induced absorption over the Himalayas calls for focused modeling and impact assessment studies to address the effects of light-absorbing aerosols, in particular BC aerosols, on the cryosphere and monsoon circulation in the decades to come especially in the context of an emerging aerosol dipole in Asia (Ramachandran et al., 2020a, 2020b).

5. Summary and conclusions

The impact of aerosols, especially the absorbing aerosols, in the Himalayan region is important for climate. We closely examine, for the first time, ground-based high-quality observations of aerosol characteristics including radiative forcing from several locations in the Indo-Gangetic Plain (IGP), the Himalayan foothills and the Tibetan Plateau, relatively poorly studied

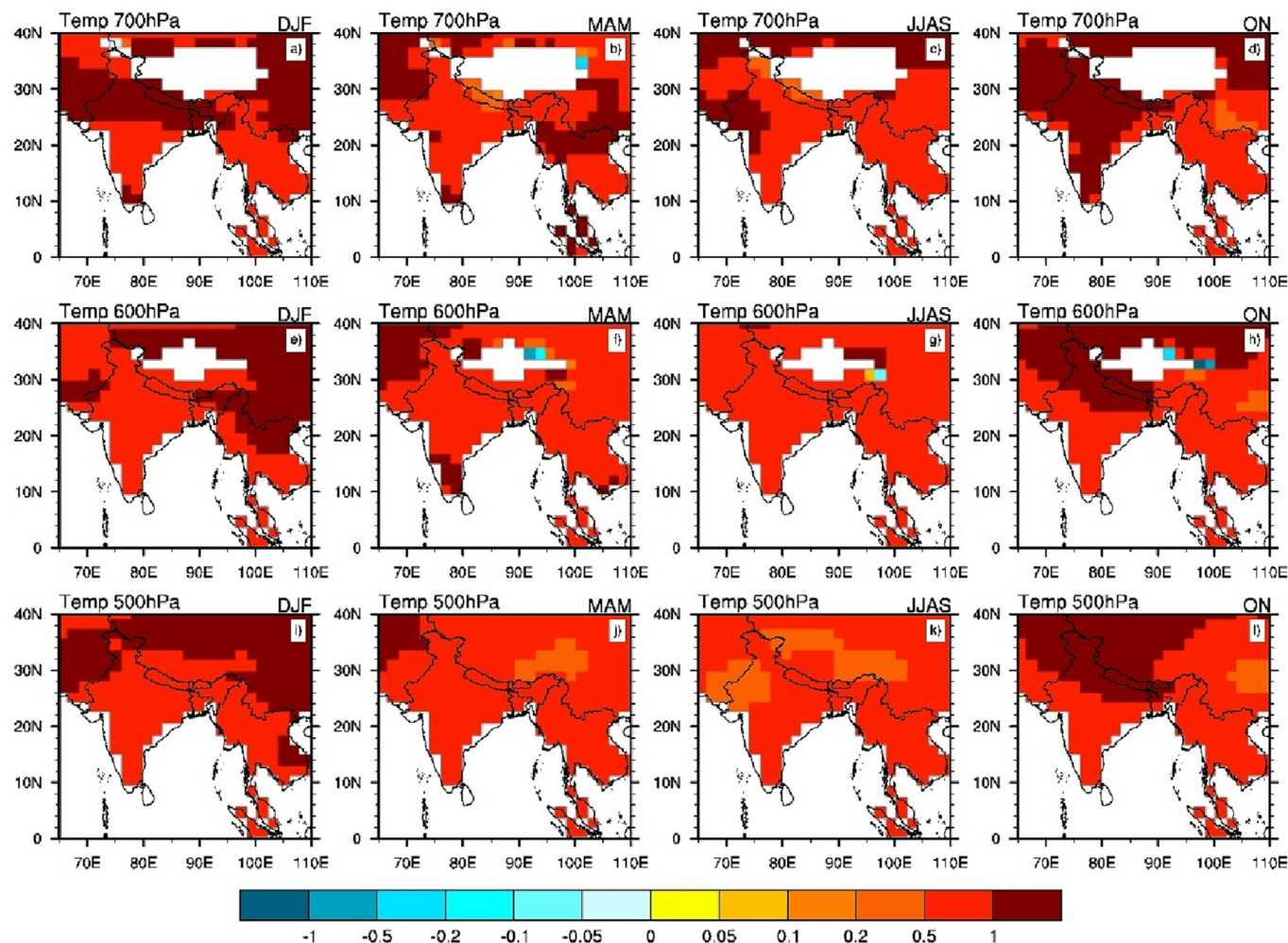


Fig. 12. The change in temperature (K) due to all forcing (includes transient emissions of aerosols, greenhouse gases (GHGs) and natural variabilities) at three altitudes across the IGP and the Himalayas simulated by UKESM1. The change in temperature corresponds to year 2014 with respect to 1850. Temperature change during winter ((a) 700 hPa (~3000 m), (e) 600 hPa (~4250 m) and (i) 500 hPa (~5500 m), pre-monsoon ((b) 700 hPa, (f) 600 hPa and (j) 500 hPa), monsoon ((c) 700 hPa, (g) 600 hPa and (k) 500 hPa), and post-monsoon ((d) 700 hPa, (h) 600 hPa and (l) 500 hPa).

regions with several sensitive ecosystems of global importance, as well as highly vulnerable large populations. This paper presents a state-of-the-art treatment of the warming that arises from these particles, using a combination of new measurements and modeling techniques. The study is novel as it combines data from multiple sources – high-quality ground-based observations along with satellite data in combination with global climate simulations – to document the aerosol radiative effects as a function of space, time and altitude over this region. Aerosol optical depth (AOD) is >0.30 at all sites confirming that this region is heavily polluted. AOD is higher over elevated locations in the Himalayas. AOD is dominated by fine mode aerosols as fine mode particles contribute $>70\%$ to total AOD. Single scattering albedo (SSA) is lower than 0.90 over Kathmandu, a metropolitan region in the Himalayan foothills, most of the year confirming the abundance of light-absorbing carbonaceous aerosols (black carbon aerosols in particular) and hence, higher absorption. Kathmandu in the Himalayas, despite being located at a higher elevation, has a lower SSA than Lumbini and Pokhara, indicating that it is likely a significant light-absorbing aerosol source to Himalayas. This finding confirms that not only the fine mode particles which are easily transported are higher at higher altitudes in the central Himalaya foothills, but they are also more absorbing in nature as they are dominated by BC, giving rise to lower SSA values than over the sites in the IGP. Furthermore, our analysis reveals that the aerosol radiative forcing efficiency (ARFE) in the atmosphere is clearly high over the IGP and the foothills of Himalayas ($80\text{--}135\text{ Wm}^{-2}$ per unit AOD), with values being

greater at higher elevations in the Himalayas. The mean ARFE is 2–4 times higher here than over other polluted sites in South and East Asia owing to higher AOD and aerosol absorption (lower SSA). Further, the observed annual mean aerosol heating rates ($0.5\text{--}0.8\text{ Kelvin/day}$), which are significantly higher than previously reported values, imply that the aerosols alone could account for $>50\%$ of the total warming (aerosols + greenhouse gases) of the lower atmosphere and surface over this region.

The aerosol radiative forcing (ARF) simulated by UKESM1 model in the CMIP6 is significantly lower than the observations over Asia, since the simulated AOD is lower, and the SSA is higher than the observations. A cooling (or lack of warming) of the lower atmosphere due to aerosols in model simulations confirms a significant underestimation of absorbing aerosols (mainly BC) in the column in the UKESM1 model, and an overestimation of scattering aerosols which masks the warming produced by absorbing aerosols significantly. Thus, it is clear that the current state-of-the-art climate models involved in CMIP6 (which were also used in the IPCC AR6) underestimate the atmospheric warming due to aerosols over the Himalaya – Tibetan Plateau (HTP) region in the lower atmosphere. This is confirmed in a recent study (Kelesidis et al., 2022) where it was shown that global climate models underpredict ARF due to BC aerosols largely due to the assumed morphology of BC, and further it was shown that light-absorption by BC aerosols was enhanced due to morphological changes, and the resultant aerosol absorption agreed well with AERONET observed BC absorption reported earlier in Ramachandran and Rupakheti

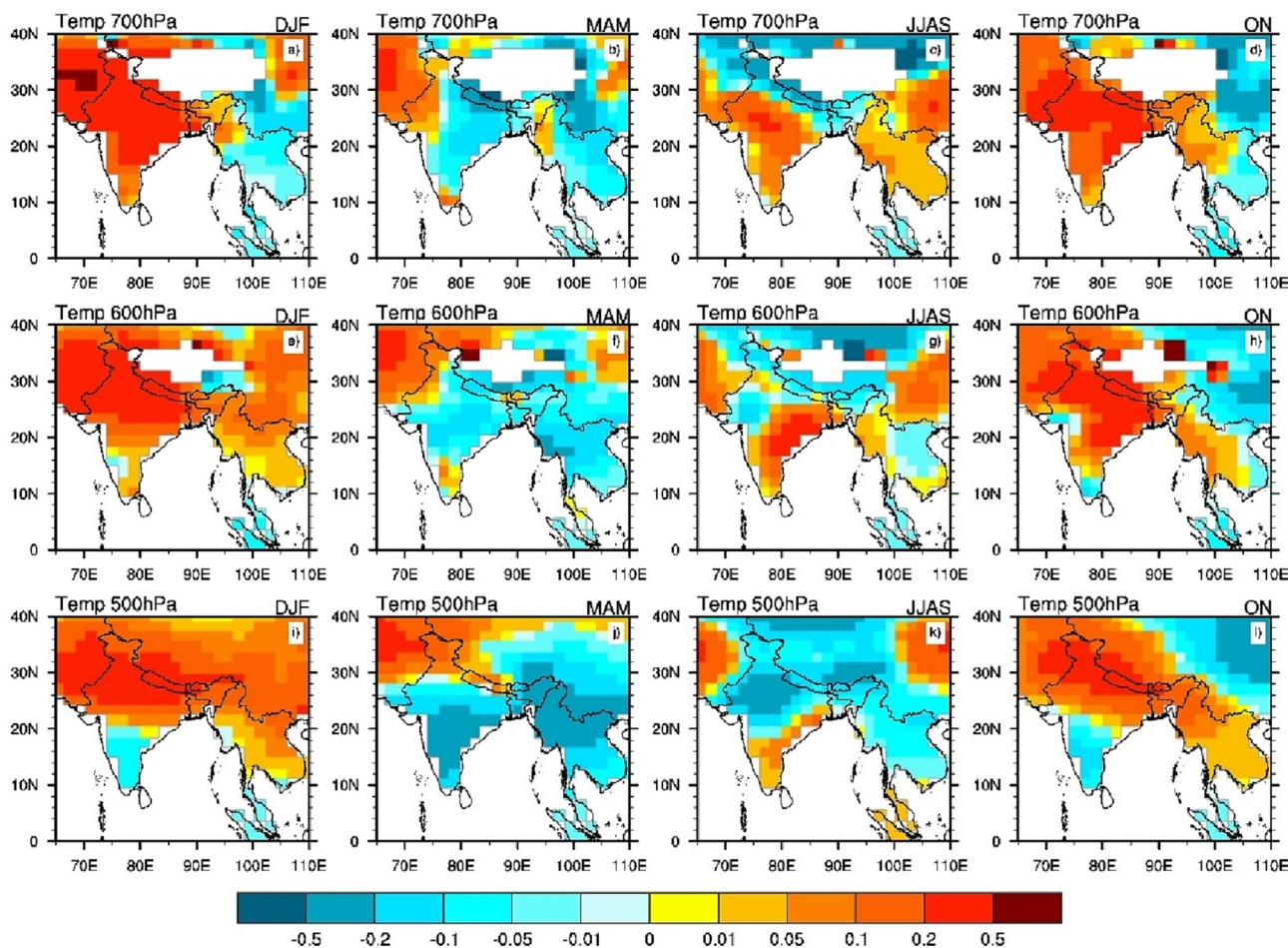


Fig. 13. The change in temperature (K) due to all aerosol forcing at three altitudes across the IGP and the Himalayas simulated by UKESM1. The change in temperature corresponds to year 2014 with respect to 1850. Temperature change during winter ((a) 700 hPa (~3000 m), (e) 600 hPa (~4250 m) and (i) 500 hPa (~5500 m)), pre-monsoon ((b) 700 hPa, (f) 600 hPa and (j) 500 hPa), monsoon ((c) 700 hPa, (g) 600 hPa and (k) 500 hPa), and post-monsoon ((d) 700 hPa, (h) 600 hPa and (l) 500 hPa).

(2020). Further, the simulations indicated that BC aerosols alone could be contributing a regional climate warming of about 1°C in the region which is consistent with our findings. The regionally coherent significant warming by aerosol absorption due to BC aerosols in the high altitudes of this region, that we observe, is a significant factor contributing to the increasing air temperature and the observed accelerated retreat of the glaciers over this region. This warming is also expected to alter atmospheric stability, and to influence the hydrological cycle and precipitation patterns, with severe consequences for the Asian summer monsoon and glaciers. Thus, we conclude that aerosols are heating up the Himalayas, and will remain a key factor driving climate change over the Hindu Kush – Himalaya – Tibetan Plateau (HKHTP) region.

Funding

The research is supported by the Research Institute for Sustainability – Helmholtz Centre Potsdam (RIFS), formerly Institute for Advanced Sustainability Studies (IASS), which is funded by the German Federal Ministry for Education and Research (BMBF) and the Brandenburg State Ministry for Science, Research and Culture (MWFK). This work was performed when SR was a Senior Fellow at IASS on a sabbatical from Physical Research Laboratory, India. He is currently an Affiliate Scholar of RIFS. R. Cherian acknowledges the funding support by the ClimXtreme project, within the framework programme of “Research for Sustainable Development (FONA3)”, by the German Federal Ministry of Education and Research (BMBF; sub-project PATTERA, FKZ 01LP1902C).

CRediT authorship contribution statement

S. Ramachandran: conceptualization, methodology, data curation, formal analysis, visualization, writing - original draft, review and editing. Maheswar Rupakheti: conceptualization, writing - review and editing. Ribu Cherian: data curation, formal analysis, visualization, writing - review and editing. Mark G. Lawrence: conceptualization, writing - review and editing.

Data availability

All the data used in the manuscript are publicly available at <https://aeronet.gsfc.nasa.gov/>, <https://psl.noaa.gov/>, <https://giovanni.gsfc.nasa.gov/giovanni/> and <https://esgf-node.llnl.gov/search/cmip6/>.

Declaration of competing interest

The authors declare no conflict of interests, including financial interests.

Acknowledgements

We used data from various publicly available data base. We thank the principal investigators of each AERONET site for their efforts in establishing and maintaining the AERONET sites (<https://aeronet.gsfc.nasa.gov/>) the data of which are used in the study. MR and MGL acknowledge Brent N. Holben from the NASA AERONET for providing two sets of CIMEL

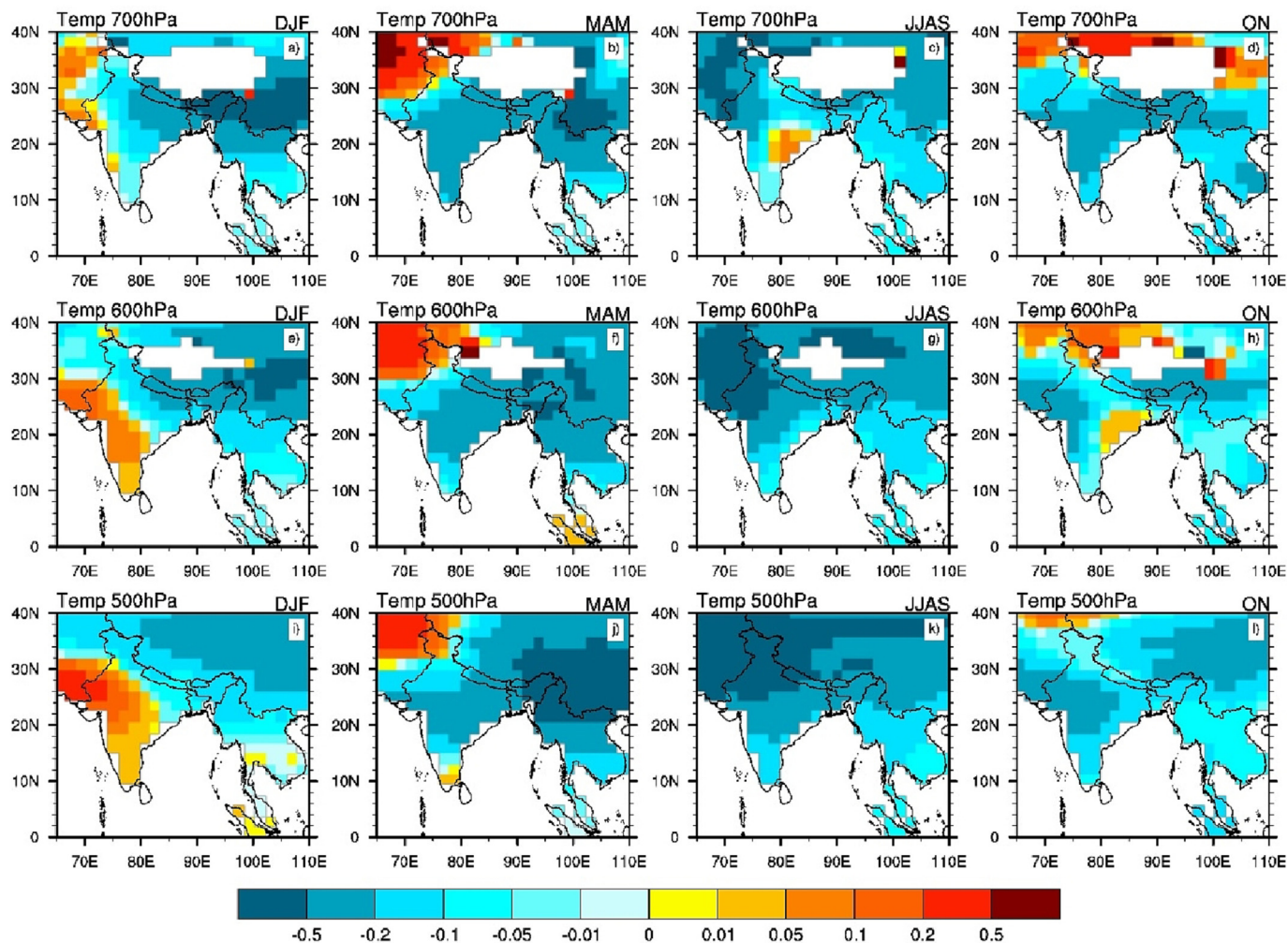


Fig. 14. The change in temperature (K) due to sulfate aerosols in the lower atmosphere across the IGP and the Himalayas simulated by UKESM1. The change in temperature corresponds to year 2014 with respect to 1850. Temperature change during winter ((a) 700 hPa (~3000 m), (e) 600 hPa (~4250 m) and (i) 500 hPa (~5500 m)), pre-monsoon ((b) 700 hPa, (f) 600 hPa and (j) 500 hPa), monsoon ((c) 700 hPa, (g) 600 hPa and (k) 500 hPa), and post-monsoon ((d) 700 hPa, (h) 600 hPa and (l) 500 hPa).

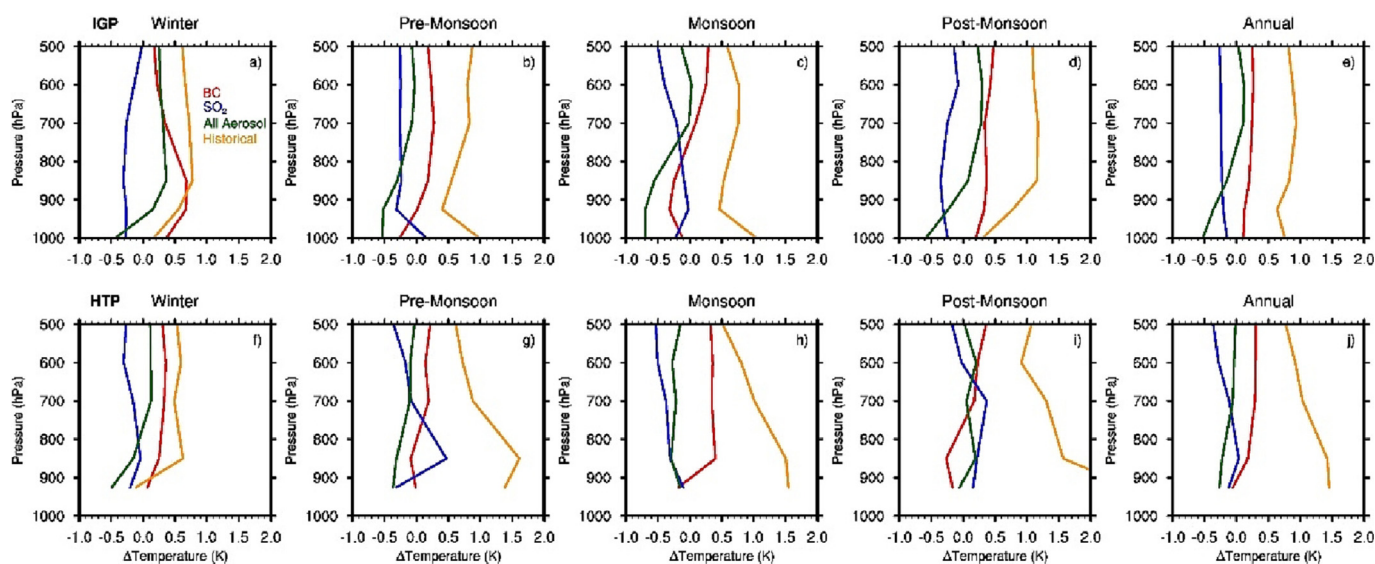


Fig. 15. The change in temperature (K) due to aerosols and greenhouse gases in the lower atmosphere over the IGP and the HTP (Fig. 1) simulated by UKESM1. The temperature change is calculated as the difference in temperature between 2014 and 1850. Temperature changes are shown due to BC, SO₂, and all aerosols, along with historical values (which include the impacts of actual transient emissions of aerosols and greenhouse gases (GHGs) and natural variabilities), on a seasonal scale over the IGP (a-d) and over the HTP (f-i), and annually for the IGP (e) and for the HTP (j).

Sun-photometers for setting up AERONET sites at Bode (Kathmandu Valley) and Lumbini. MR set up and maintained the AERONET sites at Kathmandu and Lumbini. The wind data are downloaded from NCEP Reanalysis provided by the NOAA/OAR/ESRL PSL, Boulder, Colorado, USA, from their web site at <https://psl.noaa.gov/>. Seasonal average MODIS Terra version 6.1 monthly combined dark target and deep blue AOD at 0.55 μm for land and ocean at 1° resolution, OMI OMAERUVd v003 SSA at 0.50 μm at 1° resolution, and TRMM rainfall data are downloaded from <https://giovanni.gsfc.nasa.gov/giovanni/>. We acknowledge the MODIS, OMI and TRMM mission scientists and associated NASA personnel for the production of the data used in Fig. 2. We acknowledge the climate modeling community, PCMDI, and the World Climate Data Centre, Hamburg, Germany for providing the climate model results.

References

- Abdul-Razzak, H., Ghan, S.J., 2000. A parameterization of aerosol activation: 2. Multiple aerosol types. *J. Geophys. Res.-Atmos.* 105, 6837–6844. <https://doi.org/10.1029/1999JD901161>.
- Adesina, A.J., Kumar, K.R., Sivakumar, V., Griffith, D., 2014. Direct radiative forcing of urban aerosols over Pretoria (25.75°S, 28.28°E) using AERONET Sunphotometer data: first scientific results and environmental impact. *J. Environ. Sci.* 26, 2459–2474.
- Andrews, E., Ogren, J.A., Kinne, S., Samset, B., 2017. Comparison of AOD, AAOD and column single scattering albedo from AERONET retrievals and in situ profiling measurements. *Atmos. Chem. Phys.* 17, 6041–6072. <https://doi.org/10.5194/acp-17-6041-2017>.
- Ansari, K., Ramachandran, S., 2023. Aerosol characteristics over Indo-Gangetic Plain from ground-based AERONET and MERRA-2/CAMS model simulations. *Atmos. Environ.* 293, 119434. <https://doi.org/10.1016/j.atmosenv.2022.119434>.
- Arimoto, R., Kim, Y.J., Kim, Y.P., Quinn, P.K., Bates, T.S., Anderson, T.L., Gong, S., Uno, I., Chin, M., Huebert, B.J., Clarke, A.D., Shinzuka, Y., Weber, R.J., Anderson, J.R., Guazzotti, S.A., Sullivan, R.C., Sodeman, D.A., Prather, K.A., Sokolik, I.N., 2006. Characterization of Asian dust during ACE-Asia. *Glob. Planet. Chang.* 52, 23–56.
- Barnett, T.P., Adam, J.C., Lettenmaier, D.P., 2005. Potential impact of a warming climate on water availability in snow-dominated regions. *Nature* 438, 303–309.
- Chen, P.F., Kang, S., Li, C., Zhang, Q., Guo, J., Tripathi, L., Zhang, Y., Li, G., Gul, C., Cong, Z., Wan, X., Niu, H., Panday, A.K., Rupakheti, M., Ji, Z., 2019. Carbonaceous aerosol characteristics on the third pole: a primary study based on the atmospheric pollution and cryospheric change (APCC) network. *Environ. Poll.* 253, 49–60. <https://doi.org/10.1016/j.envpol.2019.06.112>.
- Cho, C., Kim, S.-W., Rupakheti, M., Park, J.-S., Panday, A., Yoon, S.-C., Kim, J.-H., Kim, H., Jeon, H., Sung, M., Kim, B.M., Hong, S.K., Park, R.J., Rupakheti, D., Mahata, K.D., Praveen, P.S., Lawrence, M.G., Holben, B., 2017. Wintertime aerosol optical and radiative properties in the Kathmandu Valley during the SusKat-ABC field campaign. *Atmos. Chem. Phys.* 17, 12617–12632. <https://doi.org/10.5194/acp-17-12617-2017>.
- Choi, J.-O.K., Chung, C.E., 2014. Sensitivity of aerosol direct radiative forcing to aerosol vertical profile. *Tellus B* 66, 24376. <https://doi.org/10.3402/tellusb.v66.24376>.
- Collins, W.J., Lamarque, J.-F., Shulz, M., Boucher, O., Eyring, V., Hegglin, M.I., Maycock, A., Myhre, G., Prather, M., Shindell, D., Smith, S.J., 2017. AerChemMIP: quantifying the effects of chemistry and aerosols in CMIP6. *Geosci. Model Dev.* 10, 585–607. <https://doi.org/10.5194/gmd-10-585-2017>.
- Dubovik, O., King, M.D., 2000. A flexible inversion algorithm for retrieval of aerosol optical properties from sun and sky radiance measurements. *J. Geophys. Res.* 105, D16, 20,673–20,696.
- Dubovik, O., Smirnov, A., Holben, B.N., King, M.D., Kaufman, Y.J., Eck, T.F., Schuster, I., 2000. Accuracy assessments of aerosol optical properties retrieved from aerosol robotic network (AERONET) sun and sky radiance measurements. *J. Geophys. Res.* 105, 9791–9806.
- Dubovik, O., et al., 2006. Application of spheroid models to account for aerosol particle nonsphericity in remote sensing of desert dust. *J. Geophys. Res.* 111, D08. <https://doi.org/10.1029/2005JD006619>.
- Dubuisson, P., Buriez, J.C., Fouquart, Y., 1996. High spectral resolution solar radiative transfer in absorbing and scattering media: application to the satellite simulation. *J. Quant. Spec. Rad. Tran.* 55, 103–126.
- Eyring, V., Bony, S., Meehl, G.A., Senior, C.A., Stevens, B., Stouffer, R., Taylor, K.E., 2016. Overview of the coupled model Intercomparison project phase 6 (CMIP6) experimental design and organization. *Geosci. Model Dev.* 9, 1937–1958. <https://doi.org/10.5194/gmd-9-1937-2016>.
- García, O.E., Díaz, A.M., Expósito, F.J., Díaz, J.P., Dubovik, O., Dubuisson, P., Roger, J.-C., Eck, T.F., Sinyuk, A., Derimian, Y., Dutton, E.G., Schafer, J.S., Holben, B.N., García, C.A., 2008. Validation of AERONET estimates of atmospheric solar fluxes and aerosol radiative forcing by ground-based broadband measurements. *J. Geophys. Res.* 113. <https://doi.org/10.1029/2008JD012111>.
- García, O.E., Díaz, J.P., Expósito, F.J., Díaz, A.M., Dubovik, O., Derimian, Y., Dubuisson, P., Roger, J.-C., 2012. Shortwave radiative forcing and efficiency of key aerosol types using AERONET data. *Atmos. Chem. Phys.* 12, 5129–5145. <https://doi.org/10.5194/acp-12-5129-2012>.
- Gautam, R., Hsu, N.C., Tsay, S.C., Lau, K.M., Holben, B., Bell, S., Smirnov, A., Li, C., Hansell, R., Ji, Q., Payra, S., Aryal, D., Kayastha, R., Kim, K.M., 2011. Accumulation of aerosols over the Indo-Gangetic plains and southern slopes of the Himalayas: distribution, properties and radiative effects during the 2009 pre-monsoon season. *Atmos. Chem. Phys.* 11, 12841–12863. <https://doi.org/10.5194/acp-11-12841-2011>.
- Giles, D.M., Sinyuk, A., Sorokin, M.G., Schafer, J.S., Smirnov, A., Slutsker, I., Eck, T.F., Holben, B.N., Lewis, J.R., Campbell, J.R., Welton, E.J., Korokin, S.V., Lyapustin, A.I., 2019. Advancements in the aerosol robotic network (AERONET) version 3 database – automated near-real-time quality control algorithm with improved cloud screening for sun photometer aerosol optical depth measurements. *Atmos. Meas. Tech.* 12, 169–209.
- Gustafsson, O., Kruså, Zencak, Z., Sheesley, R.J., Granat, L., Engström, Praveen, P.S., Rao, P.S.P., Leck, C., Rodhe, H., 2009. Brown clouds over south Asia: biomass or fossil fuel combustion? *Science* 323, 495–498.
- Hess, M., Koepke, P., Schult, I., 1998. Optical properties of aerosols and clouds: the software package OPAC. *Bull. Amer. Met. Soc.* 79, 831–844. [https://doi.org/10.1175/1520-0477\(1998\)079](https://doi.org/10.1175/1520-0477(1998)079).
- Holben, B.N., Tarré, D., Smirnov, A., Eck, T.F., Slutsker, I., Abuhassan, N., Newcomb, W.W., Schafer, J.S., Chatenet, B., Lavenue, P., Kaufman, Y.J., Castle, J.V., Setzer, A., Markham, B., Clark, D., Frouin, R., Halthore, R., Karneli, A., O'Neill, N.T., Pietras, C., Pinker, R.T., Voss, K., Zibordi, G., 2001. An emerging ground-based aerosol climatology: Aerosol optical depth from AERONET. *J. Geophys. Res.* 106, 12067–12097.
- IPCC, 2013. In: Stocker, T.F., Qin, D., Plattner, G.-K., Tignor, M., Allen, S.K., Boschung, J., Nauels, A., Xia, Y., Bex, V., Midgley, P.M. (Eds.), Summary for Policymakers in *Climate Change 2013: The Physical Science Basis*. Contribution of Working Group I to the Fifth Assessment Report of the Intergovernmental Panel on Climate Change. Cambridge Univ. Press, Cambridge, UK and NY, USA, pp. 1–33.
- IPCC, 2021. Summary for policymakers in *climate change 2021: the physical science basis*. In: Masson-Delmotte, V., Zhai, P., Pirani, A., Connors, S.L., Péan, C., Berger, S., Caud, N., Chen, Y., Goldfarb, L., Gomis, M.I., Huang, M., Leitzell, K., Lonnoy, E., Matthews, J.B.R., Maycock, T.K., Waterfield, T., Yelekçi, O., Yu, R., Zhou, B. (Eds.), Contribution of Working Group I to the Fifth Assessment Report of the Intergovernmental Panel on Climate Change. Cambridge University Press, pp. 1–41.
- Kang, S., Zhang, Y., Qian, Y., Wang, H., 2020. A review of black carbon in snow and ice and its impact on the cryosphere. *Ear.-Sci. Rev.* 210 doi:10.1016/j.earscirev.2020.103346.
- Kedia, S., Ramachandran, S., Tripathi, S.N., Holben, B., 2014. Quantification of aerosol type, and sources of aerosols over the Indo-Gangetic Plain. *Atmos. Environ.* 98, 607–619.
- Kelesidis, G.A., Neuberger, D., Fan, L.-F., Lohmann, U., Pratsinis, S.E., 2022. Enhanced light absorption and radiative forcing by black carbon agglomerates. *Environ. Sci. Technol.* 56, 8610–8618. <https://doi.org/10.1021/asc.est.2c00428>.
- Kirilova, E.N., Marinoni, A., Bonasoni, P., Vuilleumoz, E., Facchini, M.C., Fuzzi, S., Decesari, S., 2016. Light absorption properties of brown carbon in the high Himalayas. *J. Geophys. Res.* 121, 9621–9639.
- Klimont, Z., Kupiainen, K., Heyes, C., Purohit, P., Cofala, J., Rafaj, P., Borekn-Kleefeld, J., Schöpp, W., 2017. Global anthropogenic emissions of particulate matter including black carbon. *Atmos. Chem. Phys.* 17, 8681–8723. <https://doi.org/10.5194/acp-17-8681-2017>.
- Koch, D., Schulz, M., Kinne, S., McNaughton, C., Spackman, J.R., Balkanski, Y., Bauer, S., Bernsten, T., Bond, T.C., Boucher, O., Chin, M., Clarke, A., De Luca, N., Dentener, F., Diehl, T., Dubovik, O., Easter, R., Fahey, D.W., Feichter, J., Fillmore, D., Freitag, S., Ghan, S., Ginoux, P., Gong, S., Horowitz, L., Iversen, T., Kirkevåg, Klimont, Z., Kondo, Y., Krol, M., Liu, X., Miller, R., Montanaro, V., Moteki, N., Myhre, G., Penner, J.E., Perlivitz, J., Pitari, G., Reddy, S., Sahu, L., Sakamoto, H., Schuster, G., Schwarz, J.P., Seland, Ø., Stier, P., Takegawa, N., Takemura, T., Textor, C., van Aardenne, J.A., Zhao, Y., 2009. Evaluation of black carbon estimations in global aerosol models. *Atmos. Chem. Phys.* 9, 9001–9026.
- Krishnan, R., Shrestha, A.B., Ren, G., Rajbhandari, R., Saeed, S., Sanjay, J., Syed, M.A., Vellore, R., Xu, Y., You, Q., Ren, Y., 2019. In: Wester, P., Mishra, A., Mukherji, A., Shrestha, A.B. (Eds.), Unravelling Climate Change in the Hindu Kush Himalaya: Rapid Warming in the Mountains and Increasing Extremes in The Hindu Kush Himalaya Assessment, pp. 57–97.
- Kumar, R., Barth, M.C., Pfister, G.G., Monache, L.D., Lamarque, J.F., Archer-Nicholls, S., Tilmes, S., Ghude, S.D., Wiedinmyer, C., Naja, M., Walters, S., 2018. How will air quality change in South Asia by 2050? *J. Geophys. Res.* 123, 1840–1864.
- Lam, N.L., Chen, Y., Weyant, C., Venkataraman, C., Sadavarte, P., Johnson, M.A., Smith, K.R., Brem, B.T., Arinietwe, J., Ellis, J.E., Bond, T.C., 2012. Household light makes global heat: high black carbon emissions from kerosene wick lamps. *Environ. Sci. Technol.* 46, 13531–13538.
- Lawrence, M.G., Lelieveld, J., 2010. Atmospheric pollutant outflow from southern Asia: a review. *Atmos. Chem. Phys.* 10, 11017–11096. <https://doi.org/10.5194/acp-10-11017-2010>.
- Levy, R.C., Mattoo, S., Munchak, L.A., Remer, L.A., Sayer, A.M., Patadia, F., Hsu, N.C., 2013. The collection 6 MODIS aerosol products over land and ocean. *Atmos. Meas. Tech.* 6, 2989–3034.
- Li, C., Bosch, C., Kang, S., Andersson, A., Chen, P., Zhang, Q., Cong, Z., Chen, B., Qin, D., Gustafsson, Ö., 2016. Sources of black carbon to the Himalayan-Tibetan Plateau glaciers. *Nat. Commun.* 7, 12574. <https://doi.org/10.1038/ncomms12574>.
- Liu, X.D., Chen, B.D., 2000. Climatic warming in the Tibetan Plateau during recent decades. *Int. J. Climatol.* 20, 1729–1742.
- Loeb, N.G., Doelling, D.R., Wang, H., Su, W., Nguyen, C., Corbett, J.G., Liang, L., Mitrescu, C., Rose, F.G., 2018. Clouds and the Earth's Radiant Energy System (CERES) Energy Balanced and Filled (EBAF) Top-of-Atmosphere (TOA) Edition-4.0 Data Product. *J. Climate* 31, 895–918. <https://doi.org/10.1175/jcli-d-2028.1>.
- Lüthi, Z.L., Škerlak, B., Kim, S.-W., Lauer, A., Mues, A., Rupakheti, M., Kang, S.C., 2015. Atmospheric brown clouds reach the Tibetan Plateau by crossing the Himalayas. *Atmos. Chem. Phys.* 15, 6007–6021. <https://doi.org/10.5194/acp-15-6007-2015>.
- Magi, B.I., 2011. Chemical apportionment of southern African aerosol mass and optical depth - corrigendum. *Atmos. Chem. Phys.* 11, 4777–4778. <https://doi.org/10.5194/acp-11-4777-2011>.
- Mahapatra, P.S., Puppala, P.S., Adhikary, B., Shrestha, K.L., Dawadi, D.P., Paudel, S.P., Panday, A., 2019. Air quality trends of the Kathmandu Valley: a satellite, observation and modeling perspective. *Atmos. Environ.* 201, 334–347. <https://doi.org/10.1016/j.atmosenv.2018.12.043>.

- Mallet, M., Roger, J.C., Despiou, S., Putaud, J.P., Dubovik, O., 2004. A study of the mixing state of black carbon in urban zone. *J. Geophys. Res.* 109. <https://doi.org/10.1029/2003JD003940>.
- Maurer, J.M., Schaefer, J.M., Rupper, S., Corely, A., 2019. Acceleration of ice loss across the Himalayas over the past 40 years. *Sci. Adv.* 5. <https://doi.org/10.1126/sciadv.aav7266>.
- Meehl, G.A., Arblaster, M., Collins, W.D., 2008. Effects of black carbon aerosols on the Indian monsoon. *J. Clim.* 21, 2869–2892.
- Menon, S., Hansen, J., Nazarenko, L., Luo, Y., 2002. Climate effects of black carbon aerosols in China and India. *Science* 297, 2250–2253.
- Mishchenko, M.I., Travis, L.D., Kahn, R.A., West, R.A., 1997. Modeling phase functions for dustlike tropospheric aerosols using a shape mixture of randomly oriented polydisperse spheroids. *J. Geophys. Res.* 102 (16), 831–847.
- Mulcahy, J.P., Johnson, C., Jones, C.G., Povey, A.C., Scott, C.E., Sellar, A., Turnock, S.T., Woodhouse, M.T., Abraham, N.L., Andrews, M.B., Bellouin, N., Browse, J., Carslaw, K.S., Dalvi, M., Folberth, G.A., Glover, M., Grosvenor, D.P., Hardacre, C., Hill, R., Johnson, B., Jones, A., Kipling, Z., Mann, G., Mollard, J., O'Connor, F.M., Palmieri, J., Reddington, C., Rumbold, S.T., Richardson, M., Schutgens, A.A.J., Stier, P., Stringer, M., Tang, Y., Walton, J., Woodward, S., Yool, A., 2020. Description and evaluation of aerosol in UKESM1 and HadGEM3-GC3.1 CMIP6 historical simulations. *Geosci. Model Dev.* 13, 6383–6423. <https://doi.org/10.5194/gmd-13-6383-2020>.
- Myhre, G., Aas, W., Cherian, R., Collins, W., Faluvegi, G., Flanner, M., Forster, P., Hodnebrog, Ø., Klimont, Z., Lund, M.T., Mühlensstädt, J., Myhre, C.L., Olivé, D., Prather, M., Quaas, J., Samsel, B.H., Schnell, J.L., Schultz, M., Shindell, D., Skeie, R.B., Takemura, T., Tsyro, S., 2017. Multi-model simulations of aerosol and ozone radiative forcing due to anthropogenic emission changes during the period 1990–2015. *Atmos. Chem. Phys.* 17, 2709–2720. <https://doi.org/10.5194/acp-17-2709-2017>.
- O'Neill, N.T., Eck, T.F., Smirnov, A., Holben, B.N., Thulasiraman, S., 2003. Spectral discrimination of coarse and fine mode optical depth. *J. Geophys. Res.* 108. <https://doi.org/10.1029/2002JD002975>.
- Paulot, F., Paynter, D., Ginoux, P., Naik, V., Horowitz, L.W., 2018. Changes in the aerosol direct radiative forcing from 2001 to 2015: observational constraints and regional mechanisms. *Atmos. Chem. Phys.* 18, 13265–13281. <https://doi.org/10.5194/acp-18-13265-2018>.
- Putero, D., Marinoni, A., Bonasoni, P., Calzolari, F., Rupakheti, M., Cristofanelli, P., 2018. Black carbon and ozone variability at the Kathmandu Valley and at the southern Himalayas: a comparison between a “hot spot” and a downwind high-altitude site. *Aer. Air Qual. Res.* 18, 623–635.
- Quennehen, B., Raut, J.-C., Law, K.S., Daskalakis, N., Ancellet, G., Clerbaux, C., Kim, S.-W., Lund, M.T., Myhre, G., Olivé, S., Safieddine, S., Skeie, R.B., Thomas, J.L., Tsyro, S., Bazureau, A., Belloiun, N., Hu, M., Kanakidou, M., Klimont, Z., Kupiainen, K., Myriokefalitakis, S., Quaas, J., Rumbold, S.T., Schulz, M., Cherian, R., Shimizu, A., Wang, J., Yoon, S.-C., Zhu, T., 2016. Multi-model evaluation of short-lived pollutant distributions over east Asia during summer 2008. *Atmos. Chem. Phys.* 16, 10765–10792 (2016).
- Ramachandran, S., Kedia, S., 2012. Radiative effects of aerosols over Indo-Gangetic Plains: environmental (urban vs. rural) and seasonal variations. *Environ. Sci. Poll. Res.* 19, 2159–2171.
- Ramachandran, S., Rupakheti, M., 2020. Inter-annual and seasonal variations in columnar aerosol characteristics and radiative effects over the Pokhara Valley in the Himalayan foothills – composition, radiative forcing, and atmospheric heating. *Environ. Poll.* 264, 114799. <https://doi.org/10.1016/j.envpol.2020.114799>.
- Ramachandran, S., Rupakheti, M., 2021. Inter-annual and seasonal variations in optical and physical characteristics of columnar aerosols over the Pokhara Valley in the Himalayan foothills. *Atmos. Res.* 248, 105254. <https://doi.org/10.1016/j.atmosres.2020.105254>.
- Ramachandran, S., Rupakheti, M., 2022. Trends in the types and absorption characteristics of ambient aerosols over the Indo-Gangetic plain and North China plain in last two decades. *Sci. Tot. Environ.* 832, 154867. <https://doi.org/10.1016/j.scitotenv.2022.154867>.
- Ramachandran, S., Kedia, S., Sheel, V., 2015. Spatiotemporal characteristics of aerosols in India: observations and model simulations. *Atmos. Environ.* 116, 225–244.
- Ramachandran, S., Rupakheti, M., Lawrence, M.G., 2020a. Aerosol-induced atmospheric heating rate decreases over South and East Asia as a result of changing content and composition. *Sci. Rep.* 10. <https://doi.org/10.1038/s41598-020-76936-z>.
- Ramachandran, S., Rupakheti, M., Lawrence, M.G., 2020b. Black carbon dominates the aerosol absorption over the Indo-Gangetic Plains and the Himalayan foothills. *Env. Intl.* 142, 105814. <https://doi.org/10.1016/j.envint.2020.105814>.
- Ramachandran, S., Rajesh, T.A., Cherian, R., 2021. Black carbon aerosols over source vs. background region: atmospheric boundary layer influence, potential source regions, and model comparison. *Atmos. Res.* 256, 105573. <https://doi.org/10.1016/j.atmosres.2021.105573>.
- Ramachandran, S., Rupakheti, M., Cherian, R., 2022. Insights into recent aerosol trends over Asia from observations and CMIP6 simulations. *Sci. Tot. Environ.* 807, 150756. <https://doi.org/10.1016/j.scitotenv.2021.150756>.
- Ramanathan, V., Ramana, M.V., Roberts, G., Kim, D., Corrigan, C., Chung, C., Winker, D., 2007a. Warming trends in Asia amplified by brown cloud absorption. *Nature* 448, 575–579.
- Ramanathan, V., Li, F., Ramana, M.V., Praveen, P.S., Kim, D., Corrigan, C.E., Nguyen, H., Stone, E.A., Schauer, J.J., Carmichael, G.R., Adhikary, B., Yoon, S.C., 2007b. Atmospheric brown clouds: hemispherical and regional variations in long-range transport, absorption, and radiative forcing. *J. Geophys. Res.* 112. <https://doi.org/10.1029/2006JD008124>.
- Rupakheti, D., Kang, S., Rupakheti, M., Cong, Z., Panday, A.K., Holben, B.N., 2019. Identification of absorbing aerosol types at a site in the northern edge of Indo-Gangetic Plain and a polluted valley in the foothills of the central Himalaya. *Atmos. Res.* 223, 15–23.
- Saikawa, E., Panday, A., Kang, S., Gautam, R., Zusan, E., Cong, Z., Somanathan, E., Adhikary, B., 2019. In: Wester, P., Mishra, A., Mukherji, A., Shrestha, A.B. (Eds.), *Air Pollution in the Hindu Kush Himalaya in The Hindu Kush Himalaya Assessment – Mountains, Climate Change, Sustainability and People*. Springer Nature, pp. 339–388.
- Salzmann, M., Weser, H., Cherian, R., 2014. Robust response of Asian summer monsoon to anthropogenic aerosols in CMIP5 models. *J. Geophys. Res. Atmos.* 119, 11,321–11,337. <https://doi.org/10.1002/2014JD021783>.
- Samsel, B.H., Lund, M.T., Bollasina, M., Myhre, G., Wilcox, L., 2019. Emerging Asian aerosol patterns. *Nat. Geosci.* 12, 582–586. <https://doi.org/10.1038/s41561-019-0424-5>.
- Schafer, J.S., Eck, T.F., Holben, B.N., Thornhill, K.L., Anderson, B.E., Sinyuk, A., Giles, D.M., Winstead, E.L., Ziemba, L.D., Beyersdorf, A.J., Kenny, P.R., Smirnov, A., Slutsker, I., 2014. Intercomparison of aerosol single-scattering albedo derived from AERONET surface radiometers and LARGE in situ aircraft profiles during the 2011 DRAGON-MD and DISCOVER-AQ experiments. *J. Geophys. Res. Atmos.* 119, 7439–7452. <https://doi.org/10.1002/2013JD021166>.
- Sharma, E., Molden, D., Rahman, A., Khatiwada, Y.R., Singh, S.P., Yao, T., Wester, P., 2019. Introduction to the Hindu Kush Himalaya assessment. In: Wester, P., Mishra, A., Mukherji, A., Shrestha, A.B. (Eds.), *The Hindu Kush Himalaya Assessment – Mountains, Climate Change, Sustainability and People*. Springer Nature, pp. 1–15.
- Shindell, D.T., Lamarque, J.-F., Schulz, M., Flanner, M., Jiao, C., Chin, M., Young, P.J., Lee, Y.H., Rotstayn, L., Mahowald, N., Milly, G., Faluvegi, G., Balkanski, Y., Collins, W.J., Conley, A.J., Dalsoren, S., Easter, R., Ghan, S., Horowitz, L., Liu, X., Nagashima, T., Naik, V., Rumbold, S.T., Skeie, R., Sudo, K., Szopa, S., Takemura, T., Voulgarakis, A., Yoon, J.-H., Lo, F., 2013. Radiative forcing in the ACCMIP historical and future climate simulations. *Atmos. Chem. Phys.* 13, 2939–2974. <https://doi.org/10.5194/acp-13-2939-2013>.
- Singh, A., Mahata, K.S., Rupakheti, M., Junkermann, W., Panday, A.K., Lawrence, M.G., 2019. An overview of airborne measurement in Nepal – part 1: vertical profile of aerosol size, number, spectral absorption, and meteorology. *Atmos. Chem. Phys.* 9, 245–258. <https://doi.org/10.5194/acp-19-245-2019>.
- Thompson, L.G., M.-Thompson, E., Davis, M.E., Lin, P.-N., Henderson, K., Mashiotta, T.A., 2003. Tropical glacier and ice core evidence of climate changes on annual to millennial time scales. *Clim. Chang.* 59, 137–155.
- Torres, O., Bhartiya, P.K., Jethva, H., Ahn, C., 2018. Impact of the ozone monitoring instrument row anomaly on the long-term record of aerosol products. *Atmos. Meas. Tech.* 11, 2701–2715. <https://doi.org/10.5194/amt-11-2701-2018>.
- Weissmann, M., Braun, A.F.J., Gantner, A.L., Mayr, A.G.J., Rahm, A.S., Reitebach, A.O., 2005. The Alpine Mountain-plain circulation: airborne Doppler Lidar measurements and numerical calculations. *Mon. Weather Rev.* 133, 3095–3109.
- Xu, Y., Ramanathan, V., Washington, W.M., 2016. Observed high-altitude warming and snow cover retreat over Tibet and the Himalayas enhanced by black carbon aerosols. *Atmos. Chem. Phys.* 16, 1303–1315.
- Yuan, T., Huang, J., Cao, J., Zhang, G., Ma, X., 2021. Indian dust-rain storm: possible influences of dust ice nuclei on deep convective clouds. *Sci. Tot. Env.* 779. <https://doi.org/10.1016/j.scitotenv.2021.146439>.
- Zhang, D., Zang, J., Shi, G., Iwasaka, Y., Matsuki, A., Trochkin, D., 2003. Mixing states of individual Asian particles at a coastal site of Qingdao, China. *Atmos. Environ.* 37, 3895–3901.
- Zhang, Q., Zheng, Y., Tong, D., Shao, M., Wang, S., Zhang, Y., Xu, X., Wang, J., He, H., Liu, W., Ding, Y., Lei, Y., Li, J., Wang, Z., Zhang, X., Wang, Y., Cheng, J., Liu, Y., Geng, G., Hong, C., Li, M., Liu, F., Zheng, B., Cao, J., Ding, A., Gao, J., Fu, Q., Hua, J., Liu, B., Liu, Z., Yang, F., He, K., Hao, J., 2019. Drivers of improved PM_{2.5} air quality in China from 2013 to 2017. *PNAS* 116. [www.pnas.org/cgi/doi/10.1073/pnas.1907956116](https://doi.org/10.1073/pnas.1907956116).